Journal of Aerosol Science 140 (2020) 105481

Contents lists available at ScienceDirect

Journal of Aerosol Science

journal homepage: http://www.elsevier.com/locate/jaerosci

Comparison of the predictions of Langevin Dynamics-based diffusion charging collision kernel models with canonical experiments

Li Li, Harjindar Singh Chahl, Ranganathan Gopalakrishnan *

Department of Mechanical Engineering, The University of Memphis, Memphis, TN, USA

ARTICLE INFO

Keywords:
Diffusion charging
Langevin dynamics
Unipolar
Bipolar
Collision kernel
Ion attachment coefficient

ABSTRACT

Based on the prior work of Chahl and Gopalakrishnan (2019) to infer particle-ion collision time distributions using a Langevin Dynamics (LD) approach, we develop a model for the non-dimensional particle-ion diffusion charging collision kernel β_i or H that is applicable for $0 \leq \Psi_E \leq 60,\ 0 \leq \frac{\Psi_I}{\Psi_E} \leq 1,\ Kn_D \leq 2000$ (defined in the main text). The developed model for β_i for attractive Coulomb and image potential interactions, along with the model for β_i for repulsive Coulomb and image potential interactions from Gopalakrishnan, Thajudeen, Ouyang, and Hogan (2013b), is tested against published diffusion charging experimental data. Current state of the art charging models, Fuchs (1963) and Wiedensohler (1988) regression for bipolar charging, are also evaluated and discussed. Comparisons reveal that the LD-based model accurately describes unipolar fractions for 10 – 100 *nm* particles measured in air (Adachi, Kousaka, & Okuyama, 1985), nitrogen and argon but not in helium (Adachi, Okuyama, Kousaka, Kozuru, & Pui, 1987). Fuchs model and the LD-based model yield similar predictions in the experimental conditions considered, except in helium. In the case of bipolar charging, the LD-based model captures the experimental trends quantitatively (within ±20%) across the entire size range of 4 – 40 *nm* producing superior agreement than Wiedensohler's regression. The latter systematically underpredicts charge fraction below ~20 *nm* in air (by up to 40%) for the data presented in Adachi et al. (1985). Comparison with the data of Gopalakrishnan, McMurry, and Hogan (2015), obtained in UHP air along with measurements of the entire ion mass-mobility distribution, shows excellent agreement with the predictions of the LD-based model. This demonstrates the capability to accommodate arbitrary ion populations in any background gas, when such data is available. Wiedensohler's regression, derived for bipolar charging in air using average ion mass-mobility, also describes the data reasonably well in the conditions examined. However, both models failed to capture the fraction of singly and doubly charged particles in carbon dioxide warranting further investigation.

1. Introduction

Electric charge significantly influences the growth, electrostatic drift and collective behavior of particles suspended in a gas. Accurate determination of aerosol particle charge distribution is necessary to describe aerosol dynamics (Gelbard, Tambour, & Seinfeld,

* Corresponding author.
E-mail address: rgplkrsh@memphis.edu (R. Gopalakrishnan).

https://doi.org/10.1016/j.jaerosci.2019.105481
Received 30 July 2019; Received in revised form 30 October 2019; Accepted 31 October 2019
Available online 6 November 2019
0021-8502/

List of symbols (in order of appearance)

R_i	Particle charging rate
β_i	Particle-ion collision kernel
n_p	Particle number concentration
n_i	Ion number concentration
z_p	Particle elementary charge
z_i	Ion elementary charge
N_i	Nominal ion number concentration in experiments
$\bar{t}$	Nominal residence time of particles in a unipolar charger housing
$N_i\bar{t}$	Unipolar charging parameter reported in experiments
n_{i+}	Positive ion number concentration
n_{i-}	Negative ion number concentration
m_+	Molar mass of positive ion
Z_+	Positive ion mobility
m_-	Molar mass of negative ion
Z_-	negative ion mobility
d_p	Particle diameter
a_p	Particle radius
m_i	Mass of an individual ion
T_g	Gas temperature
r^*	Distance
$\phi^*(r^*)$	Electrostatic potential energy
$e = 1.602 \times 10^{-19}\ C$	Electronic charge
$\varepsilon_o = 8.85 \times 10^{-12}\frac{F}{m}$	Permittivity of vacuum
$k_B = 1.38 \times 10^{-23}\frac{J}{K}$	Boltzmann constant
ε_r	Particle material dielectric constant
r	Non-dimensional distance
$\phi(r)$	Non-dimensional electrostatic potential energy
Ψ_E	Non-dimensional Coulomb potential energy
Ψ_I	Non-dimensional image potential energy
η_c	Continuum enhancement factor
η_f	Free molecular enhancement factor
f_i	Ion friction factor
D_i	Ion diffusion coefficient
μ_i	Ion electrical mobility
H	Non-dimensional collision kernel
Kn_D	Diffusive Knudsen number
H_{HS}	Hard sphere non-dimensional collision kernel
μ	Location parameter
A, B, C, k	Regression fit constants that appear in eq. 8b
H_{LD}	H inferred from Langevin Dynamics (LD) simulations
$H_{eq.7}$	H calculated using eq. 7
$H_{eq.8}$	H calculated using eq. 8
$H_{eq.11}$	H calculated using eq. 11
p	Particle charge
f_p	Fraction of particles carrying p charges
$\beta_{p,+}$	Collision kernel for collisions between a particle of diameter d_p carrying p charges and positive ions
$\beta_{p,-}$	Collision kernel for collisions between a particle of diameter $d_p$carrying p charges and negative ions
POS	Count of distinct positive charging ions
NEG	Count of distinct negative charging ions
θ_{i+}	Relative abundance of the i^{th} positive ion
θ_{k-}	Relative abundance of the k^{th} negative ion
$R_{p\to p+1}$	Rate of charging reaction that increases particle charge by 1
$R_{p\to p-1}$	Rate of charging reaction that decreases particle charge by 1
n_{T+}	Total concentration of positive ions in a bipolar environment
n_{T-}	Total concentration of negative ions in a bipolar environment
$\beta_{p,\pm}$	Collision kernel for particle carrying p charges and a $\pm$ ion calculated using average ion mass-mobility

f_0	Fraction of neutral particles
$1-f_0$	Fraction of charged particles
$\sum_{p>0}^{p=\infty} f_p$	Sum of positive charged fractions
$\sum_{p=-\infty}^{p<0} f_p$	Sum of negatively charged fractions
$\delta,\ \lambda,\ \eta_l,\ \alpha,\ b_{min}$	Parameters that appear in eq. 11
$d_p(nm)$	Particle diameter in *nm*
$a_i(p)$	Coefficients that appear in eq. (12) listed in Sec. S6, SI
$(\cdot)_{exp}$	Experimentally measured quantity
$(\cdot)_{eq.\ X,\ V}$	Quantity calculated using Vohra's ion properties in eq. X
$(\cdot)_{eq.X,\ M}$	Quantity calculated using Mohnen's ion properties in eq. X
$(\cdot)_{eq.12}$	Quantity calculated using eq. 12
$< p >$	Particle mean charge
UHP air	Ultra-high purity air
$\frac{f_{p=+1}}{f_{p=+2}}$	Ratio of singly to doubly charged particles of positive polarity
$\frac{f_{p=-1}}{f_{p=-2}}$	Ratio of singly to doubly charged particles of negative polarity
$\frac{f_{p=-1}}{f_{p=+1}}$	Ratio of negatively charged to positively charged particles carrying one elementary charge
$\frac{f_{p=-2}}{f_{p=+2}}$	Ratio of negatively charged particles to positively charged particles carrying two elementary charges

1979; In; Jeong & Choi, 2001; McMurry, 2000; Wu & Flagan, 1988) as well as for the inversion of particle electrical mobility data to infer measures of equivalent mobility size (Hagen & Alofs, 1983; Hogan, Li, Chen, & Biswas, 2009). The charging rate of particles R_i is evaluated as the product of the particle-ion collision kernel/collision rate coefficient/attachment coefficient β_i, the particle number concentration n_p and the ion number concentration n_i (i. e.) $R_i = \beta_i n_p n_i$. In this article we focus on the theoretical description of β_i for diffusion charging – the attachment of molecular ions driven by electrostatic forces and thermal diffusion (Brownian motion) on to aerosol particles. Within the ambit of diffusion charging of particles, we exclude effect of external electric fields (Brock, 1970b; Brock & Wu, 1973; Fjeld, Gauntt, & McFarland, 1981; Hwang & Daily, 1992; Kirsch & Zagnit'ko, 1990; Liu & Yeh, 1968; Marquard, Meyer, & Kasper, 2007; Unger, Boulaud, & Borra, 2004) and magnetic fields (Chang & Ono, 1987), high ion concentration (Adachi, Okuyama, Kousaka, Kozuru, & Pui, 1989; Marquard et al., 2007), and charging by direct impact of free electrons (O'Hara, Clements, Finney, & Davis, 1989; Romay & Pui, 1992; Ziemann, Kittelson, & McMurry, 1996; Ziemann, Liu, Kittelson, & McMurry, 1995) as beyond our scope here. We restrict our scope to the unipolar and bipolar diffusion charging of *spherical* aerosol particles and defer the consideration of particle shape (Biskos, Reavell, & Collings, 2005; Gopalakrishnan et al., 2013a, 2013b, 2015; Oh, Park, & Kim, 2004; Rogak & Flagan, 1992; Unger et al., 2004) to future investigations.

Aerosol particle charging, by virtue of the sub-μm length scales, takes place in the transition regime (Thajudeen, Gopalakrishnan, & Hogan, 2012) of ion transport wherein an ion's motion is significantly influenced by both diffusional motion (at large particle-ion separations) and inertial motion (in the immediate vicinity of the particle). To capture the potential energy driven collisions of ions with particles in the presence of background gas, development of theoretical approaches to calculate β_i for diffusion charging has received significant attention in prior work (Bricard, 1962; Chahl & Gopalakrishnan, 2019; D'Yachkov, Khrapak, Khrapak, & Morfill, 2007; Fuchs, 1963; Gatti & Kortshagen, 2008; Gopalakrishnan & Hogan, 2012; Gopalakrishnan et al., 2015; Gopalakrishnan et al., 2013a; Gopalakrishnan et al., 2013b; Hoppel & Frick, 1986; Lopez-Yglesias & Flagan, 2013; Lushnikov & Kulmala, 2004; Marlow, 1980; Ouyang, Gopalakrishnan, & Hogan, 2012; Sharma, Wang, Chakrabarty, & Biswas, 2019). Currently, the most widely used models of diffusion charging (Fuchs, 1963; Hoppel & Frick, 1986) are credited to the limiting sphere paradigm of Bricard (1962) and Fuchs (1963) and the variants therein (D'Yachkov et al., 2007; Hoppel & Frick, 1986; Lopez-Yglesias & Flagan, 2013; Lushnikov & Kulmala, 2004; Marlow, 1980; Sharma et al., 2019). β_i predicted by the limiting sphere approach has been numerously used to calculate charge distributions in the field of aerosol science and forms the basis of the widely used regression for bipolar charging developed by Wiedensohler (1988). The limiting sphere model, that calculates β_i by equating the continuum and free molecular fluxes of ions at the surface of a fictious limiting sphere around the particle, has been subjected to extensive experimental scrutiny (Adachi et al., 1985; Gopalakrishnan et al., 2015; Hussin, Scheibel, Becker, & Porstendörfer, 1983; Liu & Pui, 1974; Porstendorfer, Hussin, Scheibel, & Becker, 1984; Reischl et al., 1983, 1996; Stober, Schleicher, & Burtscher, 1991; Wiedensohler, Lutkemeier, Feldpausch, & Helsper, 1986; Wiedensohler & Fissan, 1988) in which reasonable agreement was obtained. However, a closer examination of the validation efforts suggest that in all of these cited studies (except the work of Gopalakrishnan et al. (2015)), the ion properties required to calculate β_i using the limiting sphere approach has been taken from empirical correlations (Mohnen, 1974; Vohra, Subbaramu, & Vaseduvam, 1969) for ambient ions or have been chosen to match the experimental data to produce agreement. In addition to experimental validation, inter-comparison of the limiting sphere models (D'Yachkov et al., 2007; Fuchs, 1963) against in-silico computer experiments that use a Langevin equation of motion (Chandrasekhar, 1943) to simulate dilute particle-ion collisions in the presence of a background gas has revealed several inconsistencies in the assumptions behind limiting sphere models. Gopalakrishnan and Hogan (2012) and Gopalakrishnan et al. (2013b) showed that the improper treatment of the ion's velocity and impact

parameter distributions at the surface of the limiting sphere leads to the underprediction of β_i in instances where the particle-ion potential energy is much higher than the thermal energy (for example, collision between multiply like/unlike charged particle and an ion). They also showed that even at low pressures (where inertial effects are dominant), sparse ion-neutral gas molecule collisions can contribute to increased ion flux or β_i by several orders of magnitude. This effect was neglected by Fuchs (1963) and later accounted for by Hoppel and Frick (1986) by considering a single ion-neutral collision inside the limiting sphere. Chahl and Gopalakrishnan (2019) further showed that limiting sphere approach consistently under-predicts β_i for high potential, near free molecular regime attractive Coulombic collisions, typical of highly charged particles at low pressures or singly charged sub-20 nm particles at atmospheric or low pressure. Lastly, the usage of Wiedensohler's parameterization of bipolar charge distributions using average ion properties in ambient air and limiting sphere model-derived β_i values needs to be re-evaluated as well against experiments and the predictions of competing approaches. Ion mass-mobility distributions are often approximated using average ion properties to be used in the calculation of β_i. The usage of tandem ion mobility spectrometry and mass spectrometry has allowed the measurement of the complete ion mass-mobility distributions (Gopalakrishnan et al., 2013a, 2015; Maißer, Thomas, Larriba-Andaluz, He, & Hogan, 2015). The incorporation of mass-mobility distributions to capture the contribution of multiple types of positive and negative ions to particle charging has not been examined in prior work. The usage of Wiedensohler (1988) model in gases other than air, charge estimation of sub-100 nm particles and the usage of limiting sphere approach for unipolar charge distribution calculations needs to reevaluated in unison.

An alternate approach to the limiting sphere model is through the use of Langevin Dynamics (LD) trajectory simulations develop models of β_i that parameterize the effect of pure Coulombic interactions (Chahl & Gopalakrishnan, 2019; Gopalakrishnan & Hogan, 2012), screened Coulombic interactions (Chahl & Gopalakrishnan, 2019), singular-contact image potential interactions between a neutral particle and an ion (Ouyang et al., 2012), and the effect of particle shape on unipolar diffusion charging (Gopalakrishnan et al., 2013b). LD has also been used to predict the steady state bipolar charge distribution on aerosol particles (Gopalakrishnan et al., 2013a) and grains suspended in dusty plasmas (Vaulina, Repin, & Petrov, 2006) without an explicit model for the collision kernel β_i. Gopalakrishnan et al. (2013b) developed an expression for β_i that includes the effect of the combined repulsive Coulomb and image potential interactions between a like charged particle and ion encountered during unipolar diffusion charging. However, an analogous model that includes the effect of the combined attractive Coulomb and image potential interactions between an unlike charged particle and ion encountered in bipolar diffusion charging was not developed (Gopalakrishnan et al., 2013a, 2015; Gopalakrishnan & Hogan, 2012). Recently, Chahl and Gopalakrishnan (2019), by analyzing the particle-ion collision time distribution from Langevin-inferred trajectories, parameterized the collision kernel β_i to describe the particle-ion attractive Coulombic interactions for a wide range of particle-ion electrostatic potential energy to thermal energy ratios (up to 60) and particle-ion diffusive Knudsen number (that parameterizes the ratio of the ion's mean persistence path to the particle size, up to 2000). These parameter ranges cover aerosol bipolar charging conditions for a wide space of particle size, gas pressure and ion mass-mobility combinations. Although the contribution of image potential diminishes for highly charged particles ($|z_p| >> 1$), diffusion charging of sub-micron aerosols in typical conditions lead to particle absolute charge levels $\pm 10e^-$ (Gopalakrishnan et al., 2013a; Wiedensohler, 1988) and warrants an accurate accounting of the image potential interactions for aerosol charging (Brock, 1970a; Filippov, 1993). Building on the methods of Chahl and Gopalakrishnan (2019), the *first* objective of this article is to extend their particle-ion collision kernel model to include the *combined* attractive Coulomb and image potential interactions between an unlike charged particle and ion (that is encountered in bipolar

Table 1a
Summary of unipolar charging published experiments.

Reference	Experimental parameters
Liu, Whitby, and Yu (1967)	• 1.35 μm and 0.65 μm di-octyl phthalate particles • $N_i\tilde{t}\sim 10^5\frac{s}{cm^3} - 3\times 10^7\frac{s}{cm^3}$ • Gas pressure 0.0311 – 0.96 atm
Liu and Pui (1977)	• 0.1 – 5.04 μm oleic acid particles • $N_i\tilde{t}\sim 2.56\times 10^6\frac{s}{cm^3} - 5.1\times 10^7\frac{s}{cm^3}$
Kirsch and Zagnit'Ko (1981)	• 0.043 – 0.73 μm particles • $N_i\tilde{t}\sim 10^5\frac{s}{cm^3} - 3\times 10^7\frac{s}{cm^3}$
Davison, Hwang, Wang, and Gentry (1985) and Hwang, Gentry, and Davison (1986)	• 18 nm, 24 nm, 32 nm, 42 nm silver aerosol particles • $N_i\tilde{t}\sim 10^7\frac{s}{cm^3}$
Pui, Fruin, and McMurry (1988)	• 0.004 – 0.075 μm NaCl and silver particles • $N_i\tilde{t}\sim 3\times 10^6\frac{s}{cm^3} - 1\times 10^7\frac{s}{cm^3}$
Romay, Pui, and Adachi (1991)	• 10 – 50 nm NaCl particles • 0.2 – 0.5 atm gas pressure
Adachi et al. (1985) and Adachi et al. (1987) (***used for model evaluation in this study)***	• 4 – 100 nm of zinc chloride and di-2-ethyl hexyl sebacate particles, DEHS • Background gases (air, helium, argon, nitrogen)

diffusion charging). The β_i expression described in this article, when combined with the β_i model that captures the combined repulsive Coulomb and image potential interactions described in Gopalakrishnan et al. (2013b), provides a complete set of particle-ion collision kernel β_i expressions for both attractive and repulsive Coulombic interactions, while also accounting for attractive image potential interactions. The *second* objective of this article is to compare the charge distribution predictions of the bipolar β_i model described here and unipolar β_i model described in Gopalakrishnan et al. (2013b) against published experimentally observed charge distributions in unipolar diffusion charging (Adachi et al., 1985, 1987) and bipolar diffusion charging (Adachi et al., 1985; Gopalakrishnan et al., 2015). Comparisons are also carried out with Fuchs' model (1963) and Wiedensohler's (1988) regression to ascertain which of the approaches produces better agreement with experiments and offers a robust approach to charge distribution calculation.

Table 1–A and 1-B summarize prior experimental diffusion charging studies. To test the collision kernel β_i developed by Gopalakrishnan et al. (2013b), we elect to re-analyze the unipolar charge distribution data reported by Adachi et al. (1985) and Adachi et al. (1987), that consists of an exhaustive dataset of unipolar diffusion charging by varying the particle size and background gas, along with the ion properties used. To test the collision kernel β_i developed in this article, we elect to re-analyze the bipolar charge distribution data reported by Adachi et al. (1985) and Gopalakrishnan et al. (2015). Using tandem ion mobility spectrometry-mass spectrometry, Gopalakrishnan et al. (2015) *simultaneously* measured the ion mass and mobility distributions of the charging ions generated by the bipolar charger used in that study. Detailed mobility-mass distributions were published along with the charge fractions of nominally 50 nm and 70 nm spherical gold particles as well as cylindrical gold particle of length to diameter ratio ~2 to 15. We carry out calculations of reported measured quantities using the values of ion mass and mobility, particle size and gas temperature and pressure from the same studies. Adachi et al. (1985) used two sets of ion properties (from Mohnen (1974) and Vohra et al. (1969)) to calculate theoretical expectations. We follow the same approach and calculate two sets of predictions corresponding to Mohnen (1974) and Vohra et al. (1969) as well. Gopalakrishnan et al. (2015) reported detailed tables of the mass and mobility of the ions found in their charger housing. We use the entire distribution to calculate the charging of particle by multiple singly charged positive and negative ions. For unipolar charging, Fuchs (1963) is used to compute β_i necessary for charge distribution determination and for bipolar charging, the regression Wiedensohler (1988) will be used to calculate charge distribution directly for evaluation against experimental data.

The remainder of this article is organized as follows: The *Methods* section presents a theoretical analysis of ion transport onto an aerosol particle and specifically discusses the dependence of the same on particle, ion and background gas properties. The collision kernel β_i model developed by Gopalakrishnan et al. (2013b) is briefly described. Subsequently, the β_i model development for combined attractive Coulomb and image potential based on the methods of Chahl and Gopalakrishnan (2019) is described. Subsequently, the calculation of expected aerosol particle unipolar and bipolar charge fractions for each of the experimental datasets is described along with the equations of Fuchs' model (1963) and Wiedensohler's (1988) regression. The comparison between experiments and predictions (of LD-based β_i model and other models) are discussed in the *Results and Discussion*, followed by the *Conclusions* from this study. The *Supplemental Information* (SI) published along with this article presents regression equations of the developed model, additional figures and tables to support the discussion in the main text.

2. Methods

Theoretical analysis: The collision between a spherical aerosol particle and an ion may be abstracted as the collision between a spherical collector of radius a_p and a point mass (of mass m_i and zero radius). Thus, the presented analysis may be used to describe the charging of particles with size >2 nm interacting with molecular ions in the gas-phase. The particles and ions are suspended in a

Table 1b
Summary of bipolar charging published experiments.

Reference	Experimental parameters
Hussin et al. (1983), Porstendörfer et al. (1984)	• 4 – 30 *nm* di-2-ethylhexyl-sebacate (DEHS) particles • Bipolar ions generated by the ionization of gas-phase species by α-particles originating from Am-241.
Adachi et al. (1985) (***used for model evaluation in this study)***	• 45 – 80 *nm* zinc chloride and DEHS particles • Bipolar ions generated by the ionization of gas-phase species by α-particles originating from Am-241.
Wiedensohler and Fissan (1988)	• 5 – 100 *nm* sodium chloride and silver particles in high purity argon and nitrogen
Stober et al. (1991)	• 28 – 55 *nm* silver, carbon and NaCl particles in argon and neon • Ar^+ and free electrons involved in charging
Reischl et al. (1996)	• 2.3 – 10 *nm* WO_x particles in air • fixed positive ion mass and mobility ($m_+ = 200\ amu; Z_+ = 1.33\frac{cm^2}{V.s}$) and negative ion mass and mobility ($m_- = 100\ amu; Z_- = 1.84\frac{cm^2}{V.s}$).
Gopalakrishnan et al. (2015) (***used for model evaluation in this study)***	• 51.5 *nm* and 73.2 *nm* gold particles • Ions generated by ionization using a Po-210 source • Ion mass-mobility distribution measured along with aerosol charge fractions

background gas at a common temperature of T_g. The particle concentration n_p and the ion concentrations $n_{i\pm}$ are assumed to be dilute such that the average inter-particle spacing ($n_p^{-1/3}$) and average inter-ion spacing ($n_{i\pm}^{-1/3}$) are much greater than the particle-ion interaction length scale (i. e.) the particle radius ($n_p^{-1/3}$, $n_{i\pm}^{-1/3} >> a_p$). This allows us the calculation of the particle-ion collision kernel β_i from binary interactions of the particle and ion in the presence of background gas molecules. Both the particle and ion interact with the background gas molecules via collisions that manifest as diffusion and stochastic Brownian motion of these suspended entities (Chandrasekhar, 1943). The electrostatic potential energy $\phi^*(r^*)$ between the particle and ion comprise of Coulombic potential and the polarization-induced image potential as a function of the separation r^* (Jackson, 1975):

$$\phi^*(r^*) = \frac{z_p z_i e^2}{4\pi\varepsilon_o r^*} - \frac{\varepsilon_r - 1}{\varepsilon_r + 1}\frac{z_i^2 e^2}{4\pi\varepsilon_o}\frac{a_p^3}{2r^{*2}\left(r^{*2} - a_p^2\right)} \tag{1a}$$

The thermal energy of the ion (quantified by $k_B T_g$) and the electrostatic potential energy $\phi(r^*)$ together influence the ion flux collected by the spherical particle. The interaction energy (eq. (1a)) is scaled in units of the thermal energy $k_B T_g$, distance in terms of the particle radius a_p and may be compactly expressed as:

$$\phi(r) = \frac{\phi^*(r^*)}{k_B T_g} = -\frac{\Psi_E}{r} - \frac{\Psi_I}{2r^2(r^2 - 1)} \tag{1b}$$

$\Psi_E$and Ψ_I are the electrostatic potential energy to thermal energy ratios associated with the Coulomb and image potential interactions, respectively, defined as:

$$\Psi_E = -\frac{z_p z_i e^2}{4\pi\varepsilon_o k_B T_g a_p} \tag{2a}$$

$$\Psi_I = \frac{\varepsilon_r - 1}{\varepsilon_r + 1}\frac{z_i^2 e^2}{4\pi\varepsilon_o k_B T_g a_p} \tag{2b}$$

By definition, $\Psi_E > 0$ represents unlike charged particle-ion interaction (attraction) and $\Psi_E < 0$ denotes like charged particle-ion interaction (repulsion). $\Psi_E = 0$ is the interaction between a neutral particle and ion. The image potential interaction is always attractive (Jackson, 1975) and $\Psi_I > 0$. We consider only ions that are singly charged $z_i = \pm 1$, $\Psi_I \leq |\Psi_E|$ and conducting particles ($\varepsilon_r = \infty$) but our analysis may be readily extended to non-conducting particles as well (finite ε_r).

In the continuum regime of ion transport, which is valid in the limit of the mean persistence path (Dawes & Sceats, 1988; Gopalakrishnan & Hogan, 2011; Sceats, 1986; Thajudeen et al., 2012) of the ion being much smaller than the particle radius, collision kernel β_i is well described by the equations of continuum mass transfer (Friedlander, 2000; Fuchs, 1963):

$$\beta_i = 4\pi\frac{k_B T_g}{f_i} a_p \eta_c(\Psi_E, \Psi_I) \tag{3a}$$

$$\eta_c(\Psi_E, \Psi_I) = \left(\int_1^\infty \frac{1}{r^2}\exp(\phi(r))dr\right)^{-1} \tag{3b}$$

$f_i$is the ion friction factor related to the infinite-dilution diffusion coefficient D_i via the Stokes-Einstein relation as $f_i = \frac{k_B T_g}{D_i}$ or obtained from the low-field ion mobility μ_i as $f_i = \frac{z_i e}{\mu_i}$ (Friedlander, 2000). $\eta_c(\Psi_E, \Psi_I)$ is the continuum enhancement factor that accounts for the contribution of potential interactions (eq. (1b)) to β_i in addition to diffusional transport. In the opposite regime of vacuum or ballistic transport of ions, wherein the ion mean persistence path is much longer compared to the particle size, gas kinetic theory has been employed to deduce β_i in terms of the ion's mean thermal speed $\left(\frac{8k_B T_g}{\pi m_i}\right)^{1/2}$ and particle-ion mass transfer cross-section (Allen, 1992; Mott-Smith & Langmuir, 1926; Vincenti & Kruger, 1975):

$$\beta_i = \left(\frac{8k_B T_g}{\pi m_i}\right)^{1/2} \pi a_p^2 \eta_f(\Psi_E, \Psi_I) \tag{4}$$

Analogous to the continuum enhancement factor $\eta_c(\Psi_E, \Psi_I)$, $\eta_f(\Psi_E, \Psi_I)$ is the enhancement in the particle-ion hard-sphere collision cross-section πa_p^2. $\eta_f(\Psi_E, \Psi_I)$ for combined attractive or repulsive Coulomb-image interactions is calculated using the methods described in detail elsewhere (Gopalakrishnan et al., 2013b; Ouyang et al., 2012). Eqs. (3) and (4) represent the continuum and free molecular limits of β_i. Scaling eqs. (3) and (4) with particle radius $\frac{a_p \eta_f}{\eta_c}$ as a reference length scale and the ion relaxation time $\frac{m_i}{f_i}$ as a reference timescale, yields a non-dimensional form (Gopalakrishnan & Hogan, 2012) of the collision kernel β_i as:

$$H = \frac{\beta_i m_i \eta_c}{f_i a_p^3 \eta_f^2} \tag{5a}$$

The scaling of the ion thermal energy $k_B T_g$ yields a diffusive Knudsen number, a ratio of the ion's ballistic transport timescale $\frac{a_p \eta_f}{\eta_c}\sqrt{\frac{m_i}{k_B T_g}}$ and the diffusional transport timescale $\left(\frac{a_p \eta_f}{\eta_c}\right)^2 \frac{f_i}{k_B T_g}$ (Gopalakrishnan & Hogan, 2012):

$$Kn_D = \frac{\sqrt{m_i k_B T_g}\,\eta_c}{f_i a_p \eta_f} \tag{5b}$$

The quantity $\frac{\sqrt{m_i k_B T_g}}{f_i}$ is identified as the ion mean persistence path mentioned before. Eqs. (3) and (4) expressed in non-dimensional terms represent the continuum ($Kn_D \to 0$) and freemolecular ($Kn_D \to \infty$) limits, respectively:

$$Kn_D \to 0 : H = 4\pi Kn_D^2 \tag{6a}$$

$$Kn_D \to \infty : H = \sqrt{8\pi} Kn_D \tag{6b}$$

In the next two sub-sections, we provide expressions for H or non-dimensional β_i in terms of Kn_D, Ψ_E, Ψ_I in the mass transfer transition regime – Kn_D neither too low nor too high to be described by eqs. (6a) and (6b) (Thajudeen et al., 2012). In practical terms, specification of the particle and ion properties along with gas pressure and temperature allows the determination of Kn_D, Ψ_E, Ψ_I using eqs. (2a), (2b) and (5b), respectively. The presented models for β_i cast in terms of H, allows β_i calculation via eq. (5a).

$\beta_i$model for combined repulsive Coulomb and image potential driven particle-ion collisions: In prior work, Gopalakrishnan and Hogan (2011) investigated the hard sphere ($\Psi_E = \Psi_I = 0$) collisions between a spherical particle and a point mass to derive an expression for H that converges to the limits defined by eqs. (6a) and (6b), respectively, as $Kn_D \to 0$ and $Kn_D \to \infty$:

$$H(Kn_D, \Psi_E = \Psi_I = 0) = H_{HS}(Kn_D) = \frac{4\pi Kn_D^2 + 25.836 Kn_D^3 + \sqrt{8\pi} Kn_D \left(11.211 Kn_D^3\right)}{1 + 3.502 Kn_D + 7.211 Kn_D^2 + 11.211 Kn_D^3} \tag{7}$$

Gopalakrishnan and Hogan (2012) showed that eq. (7) is accurate for all strengths of the repulsive Coulomb potential ($\Psi_E < 0$, $\Psi_I = 0$). Ouyang et al. (2012) showed that eq. (7) also describes the image potential interaction between a neutral particle and an ion when the enhancement factors $\eta_c(\Psi_E = 0, \Psi_I)$, $\eta_f(\Psi_E = 0, \Psi_I)$ are calculated appropriately. Finally, considering repulsive Coulomb and image potential simultaneously, Gopalakrishnan et al. (2013b) showed that eq. (7) is also valid for particle-ion collisions for spherical particles and non-spherical particles (the details of which are not the focus of this article). The calculations of $\eta_c(\Psi_E, \Psi_I)$, $\eta_f(\Psi_E, \Psi_I)$

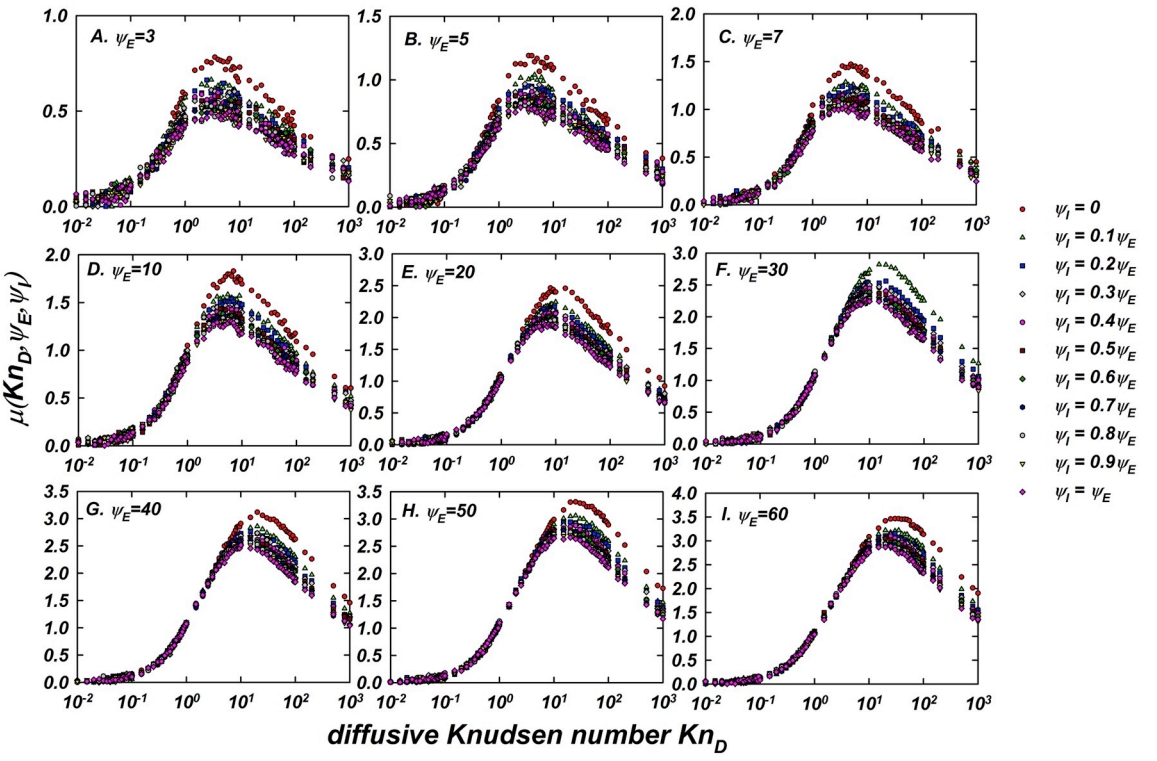

Fig. 1. Plots of the location parameter $\mu(Kn_D, \Psi_E, \Psi_I)$ for $\Psi_E = 3 - 60$ and.$0 \le \frac{\Psi_I}{\Psi_E} \le 1$

reported by Gopalakrishnan et al. (2013b) is repeated in Tables S4–A and Table S4-B, SI of this article for convenience. Thus, for unipolar (like charged particle and ion collision of either polarity) and neutral particle-ion interactions, eq. (7) may be used to calculate H or β_i.

$\beta_i$model for combined attractive Coulomb and image potential driven particle-ion collisions: Gopalakrishnan and Hogan (2012) showed that for attractive Coulomb ($\Psi_E > 0,\ \Psi_I = 0$) interactions, eq. (7) does not accurately describe H or non-dimensional β_i, especially for $\Psi_E >> \frac{3}{2}$ and near-free molecular ion transport regime ($Kn_D >> 1$). Motivated by this knowledge gap in the modeling of β_i, Chahl and Gopalakrishnan (2019) recently developed an analysis approach to parameterize attractive Coulomb interactions. Specifically, they analyzed the particle-ion collision time distributions inferred from LD trajectory simulations to parameterize H. We skip the details of their LD simulation technique to obtain a model for H valid for $0 < \Psi_E \leq 60$ and $Kn_D \leq 2000$, without considering image potential (i.e.) $\Psi_I = 0$ (Chahl & Gopalakrishnan, 2019). H_{LD} was shown to be accurately described by an equation of the form:

$$H(Kn_D, \Psi_E, \Psi_I) = e^{\mu} H_{HS}(Kn_D) \tag{8a}$$

Here, μ is a location parameter that describes the underlying distribution of $H(Kn_D, \Psi_E, \Psi_I)$ and $H_{HS}(Kn_D)$ is given by eq. (7). Firstly, in lieu of a simple Coulomb potential used by them, we employ the combined Coulomb and image potential $\phi(r)$ described by eq. (1b) and carry out LD simulations for different combinations of Kn_D, Ψ_E, Ψ_I. Fig. 1 shows the variation of the parameter μ with Kn_D, Ψ_E, Ψ_I. Following Chahl and Gopalakrishnan (2019), we summarize the values of $\mu(Kn_D, \Psi_E, \Psi_I)$ including Ψ_I, for $0 < \Psi_E \leq 60,\ 0 \leq \frac{\Psi_I}{\Psi_E} \leq 1$ and $Kn_D \leq 2000$:

$$\mu(Kn_D, \Psi_E, \Psi_I) = \frac{C}{A}\left(1 + k\frac{\log Kn_D - B}{A}\right)^{-\frac{1}{k}-1} \exp\left(-\left(1 + k\frac{\log Kn_D - B}{A}\right)^{-\frac{1}{k}}\right),\ k \neq 0 \tag{8b}$$

Regression fits to calculate $A,\ B,\ C,\ k$ as a function of Ψ_E, Ψ_I are described in Sec. S1, SI. Fig. 2 presents $H(Kn_D, \Psi_E, \Psi_I)$ for $\Psi_E = 7,\ 30,\ 60$ in panels A, B, C. For each Ψ_E, $\frac{\Psi_I}{\Psi_E} = 0,\ 0.5,\ 1$ illustrates the effect of the image potential. Also shown are the continuum and free molecular limits of H and that the simulation results agree well with these limits as $Kn_D \to 0$ (eq. (6a)) and $Kn_D \to \infty$ (eq. (6b)), respectively. In the transition regime of Kn_D, eq. (8) is used to summarize H_{LD}. The difference between the predictions of eq. (8) $H_{eq.8}$ and H_{LD}, defined as $\left(1 - \frac{H_{eq.8}}{H_{LD}}\right)\%$, is presented in panels D, E, F. Reference lines that denote difference level of ± 10% and ± 20% are also shown. It is seen that the LD-based model (eq. (8a) and eq. (8b), collectively referred to as eq. (8) hereon) describes H to within ± 10% in most cases. Figs. S2–A and Figs. S2–B present additional results for $\Psi_E = 3,\ 5,\ 10,\ 20,\ 40,\ 50$. Similar comparisons for $0 < \Psi_E \leq 60,\ 0 \leq \frac{\Psi_I}{\Psi_E} \leq 1$ and $Kn_D \leq 2000$ plotting the difference defined as $\left(1 - \frac{H_{eq.8}}{H_{LD}}\right)\%$ is presented in Fig. 3. Overall, this comparison reveals that eq. (8) describes H_{LD} nominally within ±10% for instances of particle-ion collisions where both Coulombic and image forces are significant. In instances of interaction between an uncharged particle and an ion ($\Psi_E = 0,\ 0 < \Psi_I \leq 60$), the effect of the image

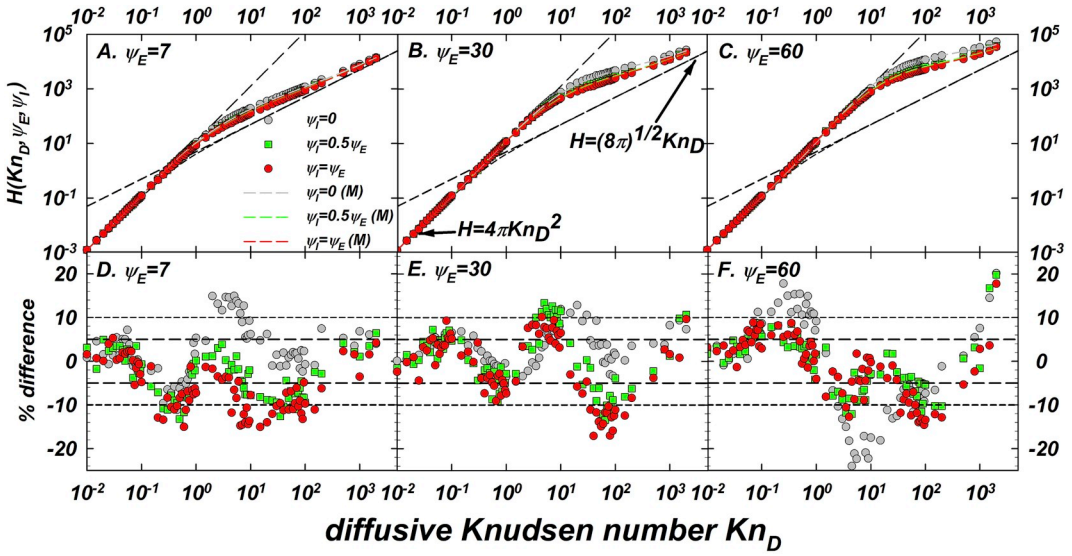

Fig. 2. Plots of the non-dimensional collision kernel $H(Kn_D, \Psi_E, \Psi_I)$ for $\Psi_E = 7$ (panel A), $\Psi_E = 30$ (panel B) and $\Psi_E = 60$ (panel C). The % difference defined as $\left(1 - \frac{H_{eq.8}}{H_{LD}}\right)\%$ for each Ψ_E is plotted in panels D, E, F. Similar results corresponding to $\Psi_E = 3,\ 5,\ 10,\ 20,\ 40,\ 50$ are presented in Figures S2-A and S2-B, SI.

potential on $\mu(Kn_D, \Psi_E = 0, \Psi_I)$ and $H(Kn_D, \Psi_E = 0, \Psi_I)$ is shown in Fig. 4. Panels A, D, G of Fig. 4 show that $\mu(Kn_D, \Psi_E = 0, \Psi_I) \cong 0$ across the entire Kn_D range investigated. As shown in panels B, E, H, the hard-sphere curve (eq. (7) or eq. (8) with $\mu = 0$) accurately describes H_{LD} to within ±5% (panels C, F, I). In total, eq. (7) and eq. (8) may be used to calculate β_i's required to calculate the complete bipolar charge distribution (with like charged and unlike charged particle-ion collisions).

Calculation of unipolar and bipolar charge distributions for comparison: To compare predicted and measured charge distributions, we use analytical expressions for calculating unipolar (Adachi et al., 1985; Boisdron & Brock, 1970) and bipolar charge distributions (Adachi et al., 1985; Hussin et al., 1983) obtained by solving population balance equations for charge conservation. For unipolar charging, the fraction f_p of particles carrying p charges when exposed to ions of ± polarity is a function of the particle-ion collision kernels $\beta_{p,\pm}$'s and the particle-ion exposure parameter $N_i\bar{t}$:

$$f_p = \begin{cases} \left(\prod_{k=p+1}^{k=0} \beta_{k,\pm}\right) \sum_{j=p}^{0} \dfrac{\exp(-\beta_{j,\pm} N_i \bar{t})}{\prod_{l=p}^{l=0} (\beta_{l,\pm} - \beta_{j,\pm})}, & p < 0 \\ l \neq j \\ \exp(-\beta_{0,\pm} N_i \bar{t}), & p = 0 \\ \left(\prod_{k=0}^{k=p-1} \beta_{k,\pm}\right) \sum_{j=0}^{p} \dfrac{\exp(-\beta_{j,\pm} N_i \bar{t})}{\prod_{l=p}^{l=0} (\beta_{l,\pm} - \beta_{j,\pm})}, & p > 0 \\ l \neq j \end{cases} \tag{9}$$

The fraction of charged particles $(1 - f_0)$ is reported as a function of background gas, particle diameter d_p and $N_i\bar{t}$ product in the unipolar diffusion charging studies selected for comparison (Adachi et al., 1985, 1987). The ion mass and mobility used by the original authors to interpret their data and for model calculations here are listed in Tables S5–A and Table S5-B, SI for various background gases considered.

To evaluate bipolar charge distributions, the solution to steady state charge conversation for a population of mono-sized particles exposed to multiple positive and negative ions yield the following equations (Adachi et al., 1985; Boisdron & Brock, 1970):

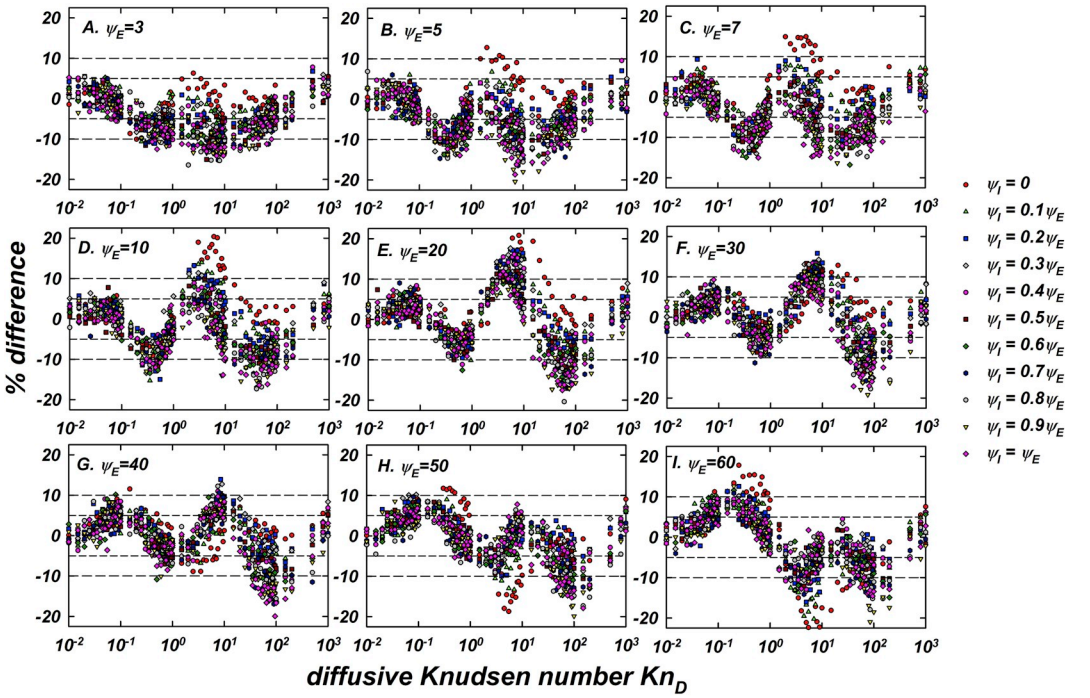

Fig. 3. Plots of the % difference defined as $\left(1 - \frac{H_{eq.8}}{H_{LD}}\right)$% for $\Psi_E = 3 - 60$ and $0 \leq \frac{\Psi_I}{\Psi_E} \leq 1$

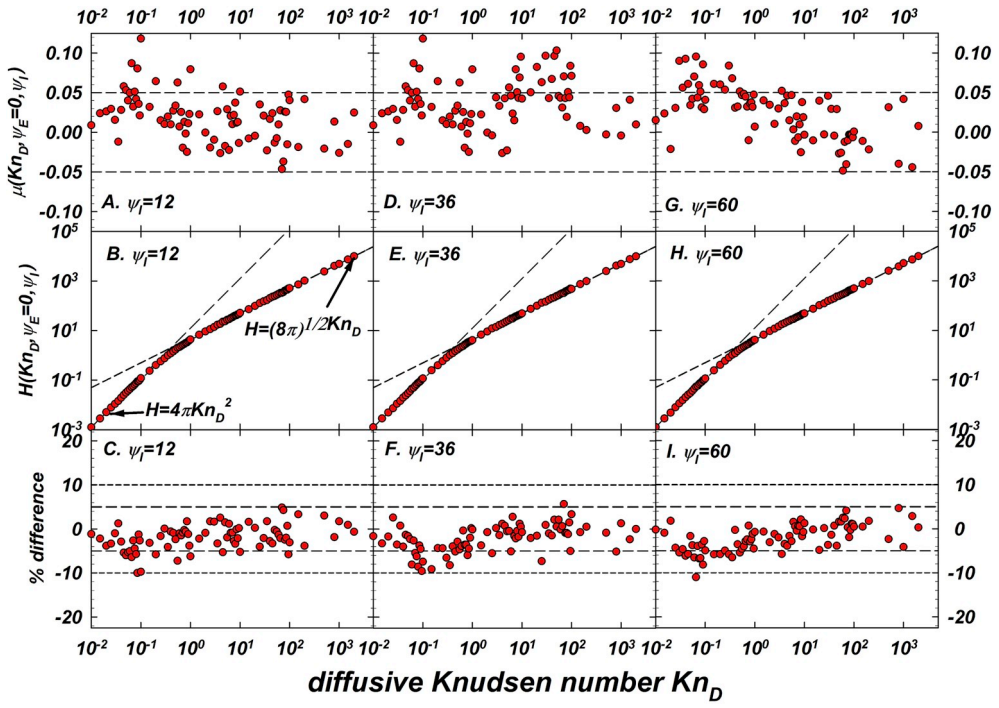

Fig. 4. Plots of $\mu(Kn_D, \Psi_E = 0, \Psi_I)$, $H(Kn_D, \Psi_E = 0, \Psi_I)$ and % difference for $\Psi_I = 12$ (panels A, B, C), $\Psi_I = 36$ (panel D, E, F) and $\Psi_I = 60$ (panel G, H, I). The % difference defined as $\left(1 - \frac{H_{eq.8}}{H_{LD}}\right)\%$ for each Ψ_I is plotted in panels C, F, I.

$$f_p = \begin{cases} \dfrac{\prod_{p=-\infty}^{p=-1}\left(\dfrac{\sum_{k=1}^{NEG}\beta_{j+1,k-}\theta_{k-}}{\sum_{i=1}^{POS}\beta_{j,i+}\theta_{i+}}\right)}{\Sigma}, & p \le -1 \\ \dfrac{1}{\Sigma}, & p = 0 \\ \dfrac{\prod_{p=1}^{p=\infty}\left(\dfrac{\sum_{i=1}^{i=POS}\beta_{j-1,i+}\theta_{i+}}{\sum_{k=1}^{NEG}\beta_{j,k-}\theta_{k-}}\right)}{\Sigma}, & p \ge 1 \end{cases} \tag{10a}$$

$$\Sigma = \sum_{p=-\infty}^{p=-1}\left\{\prod_{j=-\infty}^{j=p}\left(\frac{\sum_{k=1}^{NEG}\beta_{j+1,k-}\theta_{k-}}{\sum_{i=1}^{POS}\beta_{j,i+}\theta_{i+}}\right)\right\} + 1 + \sum_{p=1}^{p=\infty}\left\{\prod_{j=1}^{j=p}\left(\frac{\sum_{i=1}^{i=POS}\beta_{j-1,i+}\theta_{i+}}{\sum_{k=1}^{NEG}\beta_{j,k-}\theta_{k-}}\right)\right\} \tag{10b}$$

Here, $\beta_{p,i\pm}$ is the collision kernel between particles carrying p charges and the i^{th} type of $\pm$ ion. In prior work, it has been common to assume that the positive and negative ion populations may be approximated as single ion of each type whose mass and mobility are used to evaluate collision kernel for charge transfer reactions $p \to p+1$ and $p \to p-1$. A nuanced treatment of the possibility of multiple kinds of positive/negative ions is provided by the use of eq. (10) that accounts for *POS* and *NEG* number distinct types. Adachi et al. (1985), for example, assumed that a single kind of positive and negative ion each (of mass-mobility listed in Tables S5–A), to calculate charge fractions using Fuchs' model: $POS = NEG = 1$ and $\theta_+ = \theta_- = 0.5$ for comparing with Adachi et al. (1985)'s reports of $(1 - f_0), \sum_{p>0}^{p=\infty} f_p, \sum_{p=-\infty}^{p<0} f_p$ for 4–40 nm particles. Gopalakrishnan et al. (2015) report $f_0, \frac{f_{p=-1}}{f_{p=-2}}, \frac{f_{p=+1}}{f_{p=+2}}, \frac{f_{p=-1}}{f_{p=+1}}, \frac{f_{p=-2}}{f_{p=+2}}$ for 50 and 70 nm gold particles. The entire ion mass and mobility distribution for multiple charging ions and their relative abundances reported by these authors (repeated in Table S5-C, SI) are used for charge distribution calculation by accounting for multiple types of singly charged positive and negative ions. $\sum_{i=1}^{POS}\beta_{j,i+}\theta_{i+}$ represents the concentration-weighted contribution of each type of positive ion to the total charging rate (i.e.) $R_{p\to p+1} = n_p n_{T+}\sum_{i=1}^{POS}\beta_{j,i+}\theta_{i+}$. Likewise, $R_{p\to p-1} = n_p n_{T-}\sum_{k=1}^{NEG}\beta_{j,k-}\theta_{k-}$ capturing the decrease in particle charge due to collisions between particles and all of the *NEG* types of negative ions. In this work, the total concentration of positive and negative charge carriers is

assumed to be equal: $n_{T+} = n_{T-}$. Usage of eq. (10) with an appropriate model for β_i will allow the inclusion of the entire distribution to improve accuracy of predictions. In practice, the approximation of ion mass-mobility distributions as single positive and negative ion for simplicity, must be cautiously approached. It can be readily seen from eq. (10) that the rate of the charging reaction $p \rightarrow p+1$, calculated as $\sum_{i=1}^{POS} \beta_{j,i+}\theta_{i+}$ and $\langle \beta_{j,+} \rangle$ are not equal in general: $\sum_{i=1}^{POS} \beta_{j,i+}\theta_{i+} \neq \langle \beta_{j,+} \rangle$. The former accounts for the relative abundances of different kinds of positive ions and the corresponding $\beta_{j,i+}$'s. The latter $\langle \beta_{j,+} \rangle$, is the single value of the collision kernel calculated using average ion properties (mass-mobility). Ion populations have both short-lived (highly mobile) and long-lived (low mobility) ions that may contribute to charging in ambient or bipolar chargers. Using average properties can potentially overestimate the influence of highly mobile species and underestimate low mobility species. Although in the past, eq. (10) has been used with average ion properties, we recommend the incorporation of ion mass-mobility distributions into charging calculations. Maiβer et al. (2015), as a follow up to Gopalakrishnan et al. (2013a) and Gopalakrishnan et al. (2015), identified the chemical composition of positive and negative populations found in UHP air. Such an experimentally measured distribution can be easily incorporated into eq. (10). The metrics derived from the complete predicted unipolar charge distribution (f_p with $0 \leq p \leq 20$ or $-20 \leq p \leq 0$) or bipolar charge distribution (f_p with $-20 \leq p \leq 20$) are used for evaluation of LD-based β_i models given by eqs. (7) and (8).

Comparison with select existing models of diffusion charging: It is instructive to evaluate the currently used models in the field of aerosol science used to calculate charge distributions. Following Adachi et al. (1985), we repeat their comparison of the experimental unipolar charge fractions to the predictions of Fuchs' limiting sphere model (1963), cast in terms of $H(Kn_D, \Psi_E, \Psi_I)$:

$$H = \frac{4\pi Kn_D^2}{\frac{(2\pi)^{\frac{1}{2}} Kn_D \eta_f \exp(\phi(r))}{\alpha\delta^2} + \frac{\eta_c}{\eta_l}} \tag{11a}$$

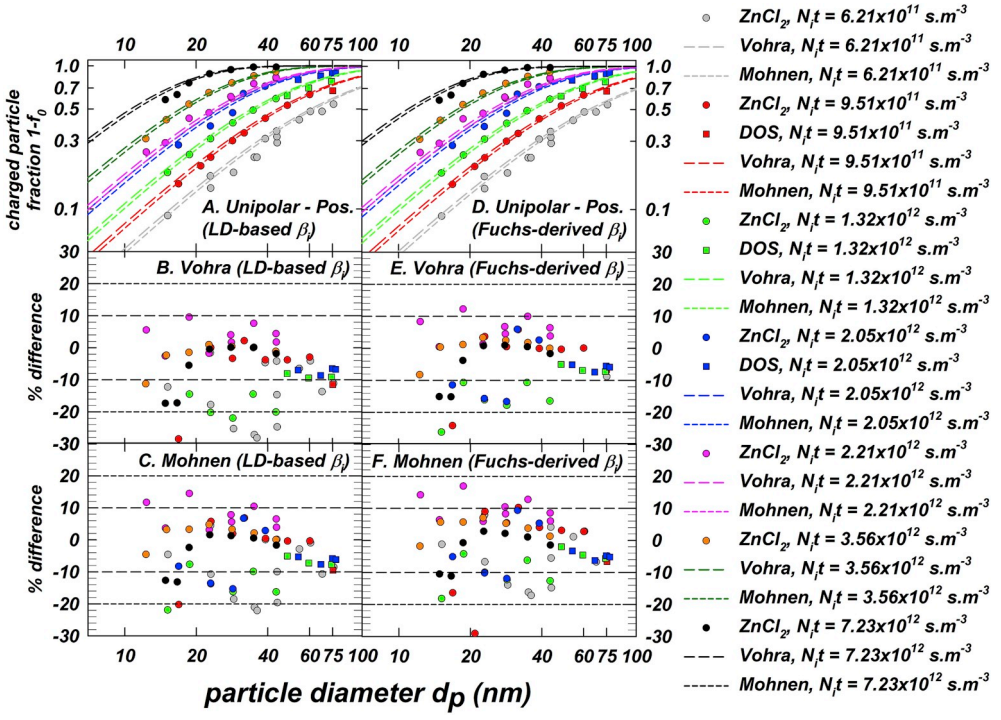

Fig. 5. A) Plot of the experimentally measured unipolar fraction of positively charged particles $(1-f_0)$ reported by Adachi et al. (1985) shown as data points of various colors and corresponding theoretical predictions using LD-based β_i (eq. (7)) in eq. (9) for two sets of ion properties (Mohnen and Vohra) shown as dashed lines. B) The % difference defined as $\left(1 - \frac{(1-f_0)_{eq.\ 7,\ V}}{(1-f_0)_{exp}}\right)$ band C) % difference defined as $\left(1 - \frac{(1-f_0)_{Eq.\ 7,\ Moh}}{(1-f_0)_{exp}}\right)$ is plotted. D) Plot of the experimentally measured $(1-f_0)$ and corresponding theoretical predictions using Fuchs-based β_i (eq. (11)) in eq. (9) for two sets of ion properties (Mohnen and Vohra) shown as dashed lines. E) The % difference defined as $\left(1 - \frac{(1-f_0)_{eq\,11,\ V}}{(1-f_0)_{exp}}\right)$ band F) % difference defined as $\left(1 - \frac{(1-f_0)_{Eq\,11,\ M}}{(1-f_0)_{exp}}\right)$ is plotted. Reference lines are shown at ±10% and ±20% and the common legend for all the panels is provided. The ion properties used in this plot is listed in Tables S5–A of the SI. (For interpretation of the references to color in this figure legend, the reader is referred to the Web version of this article.)

$$\delta = \frac{1}{\lambda}\left(\frac{1}{5}(1+\lambda)^5 - \frac{1}{3}(1+\lambda)^3\left(1+\lambda^2\right) + \frac{2}{15}\left(1+\lambda^2\right)^{\frac{5}{2}}\right) \tag{11b}$$

$$\eta_l = \left(\int_{\delta}^{\infty} \frac{1}{r^2}\exp(\phi(r))dr\right)^{-1} \tag{11c}$$

$$\lambda = 1.329\left(\frac{\pi}{8}\right)^{\frac{1}{2}}\frac{Kn_D\eta_f}{\eta_c} \tag{11d}$$

$$\alpha = \left(\frac{b_{min}}{\delta}\right)^2 \tag{11e}$$

Here, b_{min} is the minimum value for the function: $b(r) = r\left(1 + \frac{2}{3}(\phi(\delta) - \phi(r))\right)^{\frac{1}{2}}$ in the region $r = 1$ to $r = \delta$ and $\phi(r)$ is given by eq. (1b). Eq. (11) is used in eq. (9) to calculate expected unipolar charge fractions for each data set in addition to LD-based eq. (7). Predictions of each model are labeled in figures as "LD-based β_i" and "Fuchs-derived β_i" using Mohnen/Vohra ion properties as discussed shortly.

To calculate bipolar charge distributions, we elect to present comparisons of the experimental data with the widely used regression expression put forward by Wiedensohler (1988):

$$1nm \le d_p \le 20nm : f_p = \begin{cases} 10^{\left[\sum_{i=0}^{5} a_i(p)\cdot\left\{log_{10}\left(d_p(nm)\right)\right\}^i\right]}, & p = -1,\ 0,\ 1 \\ 0, & p = -2,\ 2 \end{cases} \tag{12a}$$

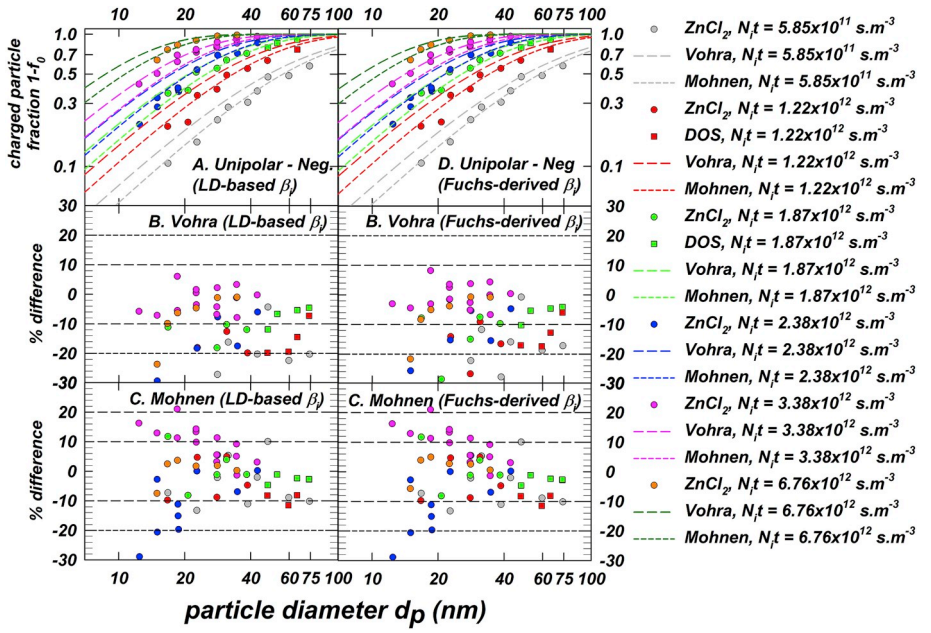

Fig. 6. A) Plot of the experimentally measured unipolar fraction of negatively charged particles $(1 - f_0)$ reported by Adachi et al. (1985) shown as data points of various colors and corresponding theoretical predictions using LD-based β_i (eq. (7)) in eq. (9) for two sets of ion properties (Mohnen and Vohra) shown as dashed lines. B) The % difference defined as $\left(1 - \frac{(1-f_0)_{eq.\ 7,\ V}}{(1-f_0)_{exp}}\right)$ band C) % difference defined as $\left(1 - \frac{(1-f_0)_{Eq.\ 7,\ M}}{(1-f_0)_{exp}}\right)$ is plotted. D) Plot of the experimentally measured $(1 - f_0)$ and corresponding theoretical predictions using Fuchs-based β_i (eq. (11)) in eq. (9) for two sets of ion properties (Mohnen and Vohra) shown as dashed lines. E) The % difference defined as $\left(1 - \frac{(1-f_0)_{eq\,11,\ V}}{(1-f_0)_{exp}}\right)$ band F) % difference defined as $\left(1 - \frac{(1-f_0)_{Eq\,11,\ M}}{(1-f_0)_{exp}}\right)$ is plotted. Reference lines are shown at and ±20% and the common legend for all the panels is provided. The ion properties used in this plot is listed in Tables S5–A of the SI. (For interpretation of the references to color in this figure legend, the reader is referred to the Web version of this article.)

$$20nm < d_p \le 1000nm : f_p = 10^{\left[\sum_{i=0}^{5} a_i(p)\cdot\left\{log_{10}\left(d_p(nm)\right)\right\}^i\right]},\ p = -2, -1,\ 0,\ 1,\ 2 \tag{12b}$$

The parameterization of charge fraction (eq. (12)) was derived based on β_i's calculated using Hoppel and Frick (1986)'s variant of the limiting sphere model. Eq. (12) will be used to directly calculate bipolar charge fractions as a function of particle size d_p without calculating β_i. The coefficients $a_i(p)$ are tabulated in Sec. S6, SI.

3. Results and discussion

Unipolar diffusion charging comparisons: Adachi et al. (1985) present data of the unipolar charging of zinc chloride and dioctyl sebacate (DOS) particles by unipolar positive and negative ions. Fig. 5 shows the experimental measurements of $(1-f_0)$ by Adachi et al. (1985), particle charging by *positive* ions, shown as discrete data points of various colors in Fig. 5-A and 5-D. The $N_i\bar{t}$ parameter varies from $6.2\times10^{11}\frac{s}{m^3} - 7.2\times10^{12}\frac{s}{m^3}$ in these measurements. The theoretical expectations calculated using eq. (9) with β_i's derived from eq. (7) are shown as dashed lines in Fig. 5-A, and using Fuchs's limiting sphere model (eq. (11)) in Fig. 5-D, for two sets of ion properties derived from Mohnen (1974) and Vohra et al. (1969). The % difference between $(1-f_0)_{exp}$ and $(1-f_0)_{eq.\ 7,\ V}$ is presented in Fig. 5-B and the % difference between $(1-f_0)_{exp}$ and $(1-f_0)_{eq.\ 7,\ M}$ is presented in Fig. 5-C. The % difference in each case (using eq. (7)) is calculated as $\left(1-\frac{(1-f_0)_{eq.\ 7,V}}{(1-f_0)_{exp}}\right)$% and $\left(1-\frac{(1-f_0)_{eq.\ 7,\ M}}{(1-f_0)_{exp}}\right)$%, respectively. Correspondingly, the % difference between the predictions using Fuchs theory (eq. (11)), $(1-f_0)_{eq.11,\ V}$ and $(1-f_0)_{eq.11,\ M}$, and experimental data are plotted in Fig. 5-E and 5-F. From the comparison, it can be observed that the predictions using both Vohra's and Mohnen's ion properties are within ±10% for most of the datapoints for both models considered here. The models overpredict the experiments to a small extent but nominally, the difference is no larger than 10% in either direction, validating the charging model of eq. (7) (Gopalakrishnan et al., 2013b) that we test here. Fuchs'

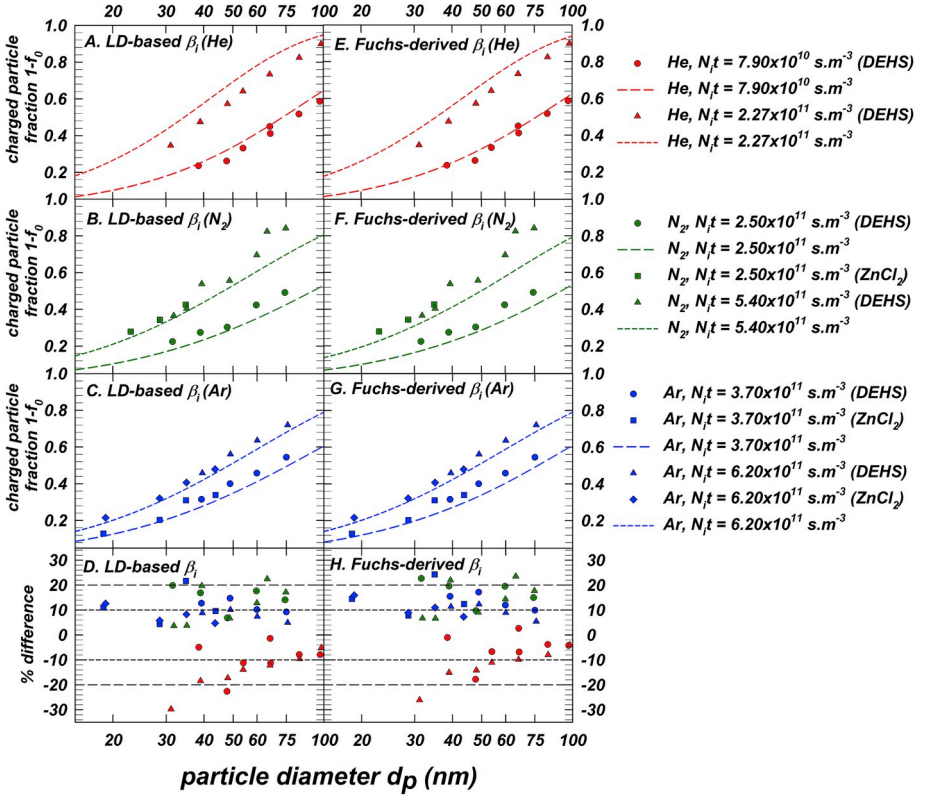

Fig. 7. Plot of the experimentally measured unipolar fraction of positively charged particles $1-f_0$ reported by Adachi et al. (1987) for various gases shown as data points of red color for *He* (panels A, E), green color for N_2 (panels B, F) and blue color for *Ar* (panels C, G). Corresponding theoretical predictions using LD-based β_i (eq. (7) in eq. (9)) with the ion properties listed in Table S5-B, SI are shown as dashed lines of the same color in panels A, B, C. Theoretical predictions using Fuchs-derived β_i (eq. (7) in eq. (9)) are shown as dashed lines in panels E, F, G. The % difference defined as $\left(1-\frac{(1-f_0)_{eq.\ 7}}{(1-f_0)_{exp}}\right)$ is plotted along with reference lines at ±10% and ±20% in panel D for LD-based β_i and panel H for Fuchs-derived β_i. (For interpretation of the references to color in this figure legend, the reader is referred to the Web version of this article.)

limiting sphere model that was originally used by Adachi et al. (1985) to interpret their measurements, and the LD-based model (eq. (7)) advanced here make similar predictions for ions in air. This trend is seen in the case of unipolar charging of particles by negative ions as well, shown in Fig. 6, for $N_i\bar{t} \sim 5.9 \times 10^{11} \frac{s}{m^3} - 6.8 \times 10^{12} \frac{s}{m^3}$. Theoretical predictions emulate the data quite well as seen from Fig. 6-A. Fig. 6-B and 6-C show the corresponding % differences between LD-based model predictions and experiments defined for Fig. 5 previously. Like in the case of positive ions, the % difference here is seen to be within ±10% with a few data points outside for both LD-based model (eq. (7)) and Fuchs (eq. (11)). Overall, the charging model eq. (7) of Gopalakrishnan et al. (2013b) reliably predicts the experimentally-observed charged particle fraction in the unipolar charging measurements of Adachi et al. (1985). Fig. 6-D, 6-E, 6-F also show a similar trend and that shows that LD-model and Fuchs model yield practically identical predictions of unipolar charge fractions in air for sub-100 nm particles. Further comparison with the charging of particles by ions derived by the direct ionization of inert gas molecules (He^+, N_2^+, Ar^+) is shown in Fig. 7. Fig. 7-A shows $(1-f_0)$ measured in *He* by Adachi et al. (1987) shown as datapoints along with theoretical expectations for $(1-f_0)_{eq.\ 7}$ shown as dashed lines for two values of the $N_i\bar{t}$ parameter. Even though two materials were examined in the study (zinc chloride and DEHS), our data analysis assumed conducting particle and thereby produced a single prediction for $(1-f_0)_{eq.\ 7}$ for both these materials. Fig. 7-B and Fig. 7-C present data and theoretical curves using eq. (7) in eq. (9) for N_2 (green filled triangles/circles/squares and dashed lines) and *Ar* (blue filled triangles/circles/squares/diamonds and dashed lines), respectively, with the % difference between $(1-f_0)_{exp}$ and $(1-f_0)_{eq.\ 7}$ is shown in Fig. 7-D with reference lines at ± 10% , ±20% for all the experimental values plotted in Fig. 7-A, 7-B, 7-C. Likewise, Fig. 7-E (*He*), 7-F (N_2) and 7-G (*Ar*) plot the predictions of Fuchs model (eq. (11)) along with experimental data. The corresponding % difference between $(1-f_0)_{exp}$ and $(1-f_0)_{eq.\ 11}$ is shown in Fig. 7-H for all three gases considered. As it is clearly evident, most of the datapoints fall within ±20% of the experimental data with a few outliers without any obvious explanation. While ions in air (Figs. 5 and 6), nitrogen and argon show relatively low systematic bias in the % difference, measurements in helium disagree one-sidedly with theoretical predictions. It is seen that neither model

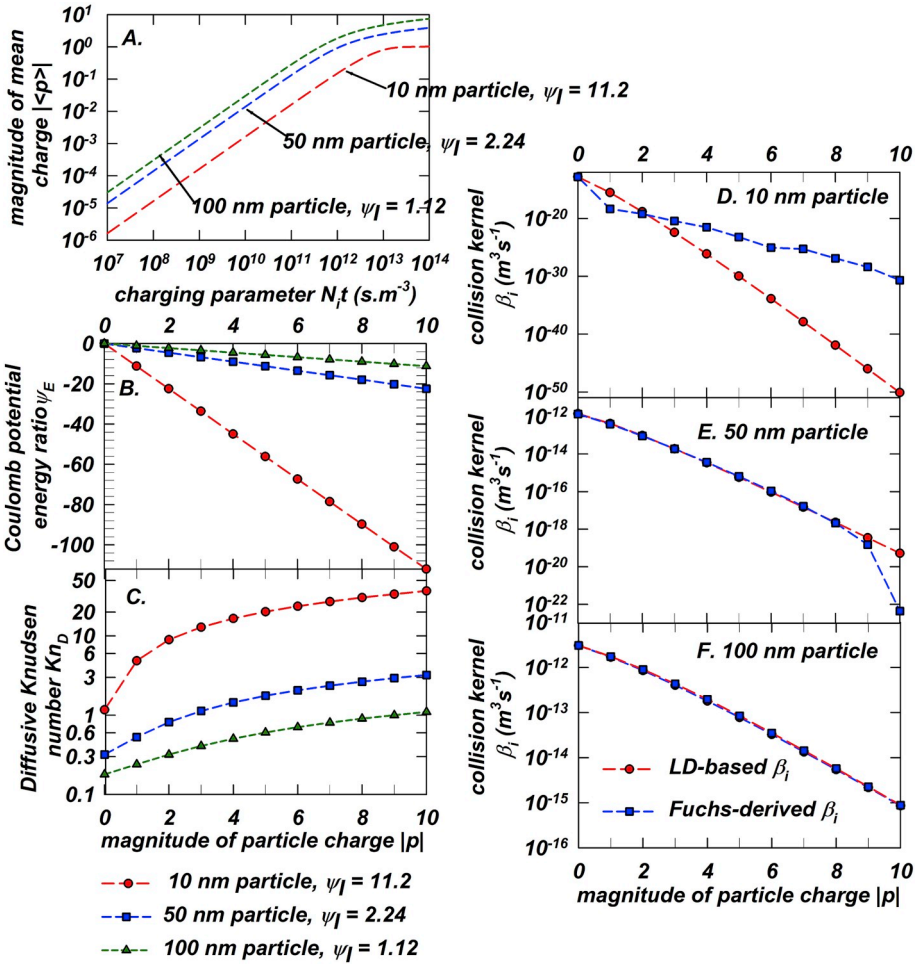

Fig. 8. A) Calculated mean charge for 10, 50, 100 nm particles exposed to N_2^+ ions in N_2 as a function of the $N_i\bar{t}$ product. B) Variation of the Coulomb potential energy ratio and C) the particle-ion diffusive Knudsen number as a function of the particle charge. Panels D, E, F show β_i predictions of LD model (eq. (7)) and Fuchs model (eq. (11)) for collisions between particles carrying *p* units of charge and a like charged ion.

quantitatively captures the variation in the charge particle fraction in helium. This needs to be further investigated in future studies considering the mobility of ions formed in helium and the high mean thermal speed of helium atoms.

Along with the good agreement with the unipolar charging data of Adachi et al. (1985), we find that the agreement between theoretical predictions with β_i's derived from both models (eq. (7) and eq. (11)) to be excellent (except in helium) taking into account the nominal experimental uncertainty of ~10% with the reported data. To understand the agreement between the two models, we calculated several parameters related to the unipolar charge distribution of particles. Fig. 8 presents calculations of the magnitude of the mean charge $|< p >|$ (panel 8-A) for 10 nm, 50 nm, 100 nm conducting particles in N_2 at 298 K and 1 atm. The $N_i\bar{t}$ was varied from $10^7 - 10^{14}\frac{s}{m^{-3}}$ for ions with mobility of $1.87 \times 10^{-4}\frac{m^2}{s.V}$ and mass of $0.028\frac{kg}{mole}$. The Coulomb potential energy ratio Ψ_E (Fig. 8-B) and the diffusive Knudsen number Kn_D (Fig. 8-C) encountered in the unipolar charging of particles as a function of the particle charge magnitude $|p|$ is also plotted. It is seen that Kn_D~30 for 10 nm, ~3 for 50 nm and ~1 for 100 nm particles, that represent transition to near free-molecular regime of ion transport. Panels 8-D, 8-E and 8-F present the collision kernel β_i calculated using LD-based model (eq. (7))

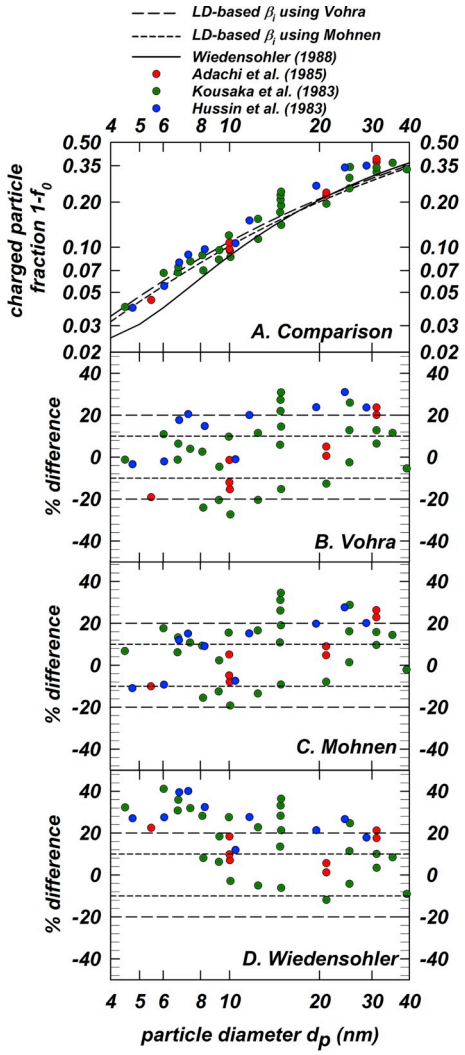

Fig. 9. A) Plot of the experimentally measured bipolar fraction of $(1 - f_0)$ reported by Adachi et al. (1985), Kousaka et al. (1983) and Hussin et al. (1983) shown as data points of various colors and corresponding theoretical predictions (using eq. (7) & eq. (8) in eq. (10)) for two sets of ion properties (Mohnen and Vohra) shown as dashed black lines and Wiedensohler's regression (eq. (12)) as a solid black line. B) The % difference defined as $\left(1 - \frac{(1-f_0)_{eq.\ 7,eq.8.\ Vohra}}{(1-f_0)_{exp}}\right)$ between predictions using Vohra's ion properties is plotted. C) The % difference defined as $\left(1 - \frac{(1-f_0)_{eq.\ 7,eq.8.\ M}}{(1-f_0)_{exp}}\right)$ between predictions using Mohnen's ion properties is plotted. D) The % difference defined as $\left(1 - \frac{(1-f_0)_{eq.\ 12}}{(1-f_0)_{exp}}\right)$ between Wiedensohler's regression is plotted. Reference lines are shown at ±10% and ±20%. The ion properties used in this plot are listed in Tables S5–A of the SI. (For interpretation of the references to color in this figure legend, the reader is referred to the Web version of this article.)

and Fuchs model (eq. (11)). It is interesting to note that for $|p| < \sim 3$ or/and for $Kn_D < \sim 1$, the two models predict the similar values of β_i. From the mean charge plotted in Fig. 8-A, it is seen that at an $N_i\bar{t} = 10^{12}\frac{s}{m^{-3}}$, the mean charge of particles $\leq \sim 2$. In these conditions (that is typical of the measurements used here for model validation), the presence of higher charge levels ($|p| > 5$) is expected to be minimal and that the two models are similar. However, prior comparisons of LD-based β_i and Fuchs (limiting sphere model)-derived β_i, by Gopalakrishnan et al. (2013b) for repulsive Coulomb interactions and by Chahl and Gopalakrishnan (2019) for attractive Coulomb interactions, reveal that at high values of Ψ_E (higher charge states) limiting sphere model leads to inconsistent (non-monotonic) predictions that arise to improper treatment of the ion velocity and impact parameters in the limiting sphere model formulation. While the disagreement between LD-based β_i and Fuchs-derived β_i at $|\Psi_E| > \frac{3}{2}$ is elaborated elsewhere (Chahl & Gopalakrishnan, 2019; Gopalakrishnan & Hogan, 2012), we infer that under the experimental conditions considered, eq. (7) and eq. (11) produced *practically similar* charge distributions. We expect measurements of charge fractions at higher $N_i\bar{t}$ to reveal significant deviations and such experiments are necessary to test both the models and delineate any differences, especially in high potential energy (high Ψ_E) driven diffusion charging at high Kn_D. Eq. (7) was also shown to be valid for non-spherical particles as well by Gopalakrishnan et al. (2013b);

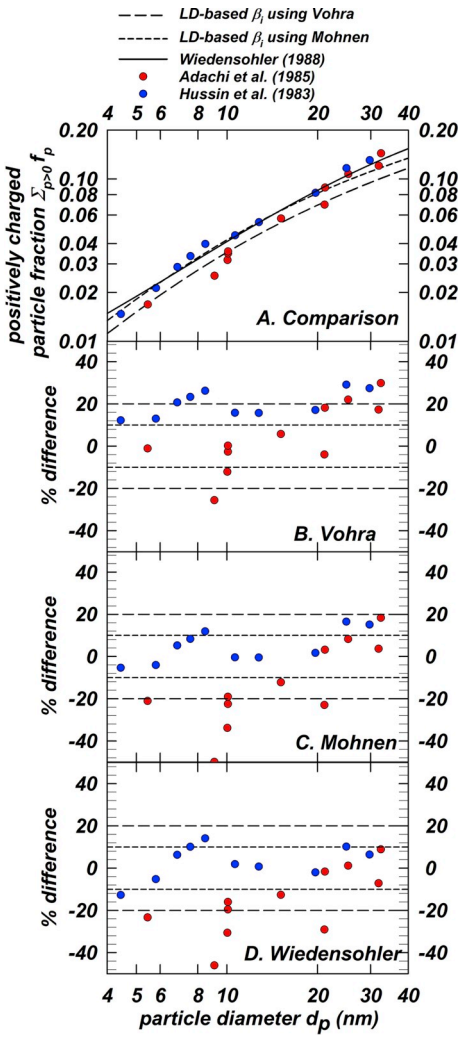

Fig. 10. A) Plot of the experimentally measured bipolar fraction of $\sum_{p>0}^{p=\infty} f_p$ reported by Adachi et al. (1985), Kousaka et al. (1983) and Hussin et al. (1983) shown as data points of various colors and corresponding theoretical predictions (using eq. (7) & eq. (8) in eq. (10)) for two sets of ion properties (Mohnen and Vohra) shown as dashed black lines and Wiedensohler's regression (eq. (12)) as a solid black line. B) The % difference defined as $\left(1 - \frac{(\sum_{p>0}^{p=\infty} f_p)_{eq.\ 7,eq.8,\ V}}{(\sum_{p>0}^{p=\infty} f_p)_{exp}}\right)$ between predictions using Vohra's ion properties is plotted. C) The % difference defined as $\left(1 - \frac{(\sum_{p>0}^{p=\infty} f_p)_{eq.\ 7,eq.8,\ M}}{(\sum_{p>0}^{p=\infty} f_p)_{exp}}\right)$ between predictions using Mohnen's ion properties is plotted. D) The % difference defined as $\left(1 - \frac{(\sum_{p>0}^{p=\infty} f_p)_{eq.\ 12}}{(\sum_{p>0}^{p=\infty} f_p)_{exp}}\right)$ between Wiedensohler's regression is plotted. Reference lines are shown at ±10% and ±20%. The ion properties used in this plot are listed in Tables S5–A of the SI. (For interpretation of the references to color in this figure legend, the reader is referred to the Web version of this article.)

considering this and the suitability of Fuchs model (eq. (11)) for only spherical shaped particles, eq. (7) may be advantageously used to describe the charging of any shaped particles across the entire diffusive Knudsen number based transport regime. The experimental testing of eq. (7) for nonspherical particles, however, needs to be carried out in future studies. For spherical particles, Fuchs' limiting sphere model (1963) is also accurate based on the comparisons shown here.

Bipolar diffusion charging comparisons: Adachi et al. (1985) report measures of the bipolar charge distribution and also summarized prior measurements of Hussin et al. (1983) and Kousaka, Adachi, Okuyama, Kitada, and Motouchi (1983). They used positive and negative ion mass-mobility from both Mohnen (1974) and Vohra et al. (1969) to compare their experiments using the Fuchs' charging model (1963). We follow their approach for comparison with charge fractions predictions using eq. (10) with LD-based β_i (eqs. (7) and (8)) and charge fractions calculated using Wiedensohler (1988)'s expression (eq. (12)). Fig. 9-A shows $(1 - f_0)$: measured values as datapoints of red/green/blue, black dashed lines corresponding to predictions using Mohnen (1974) and Vohra et al. (1969)'s ion properties and a solid dashed line (eq. (12)). The choice of ion properties (Mohnen/Vohra) has a minimal influence on $1 - f_0$ and the qualitative trend of the data is captured well by the model predictions using both sets of ion properties. Quantitative agreement is seen

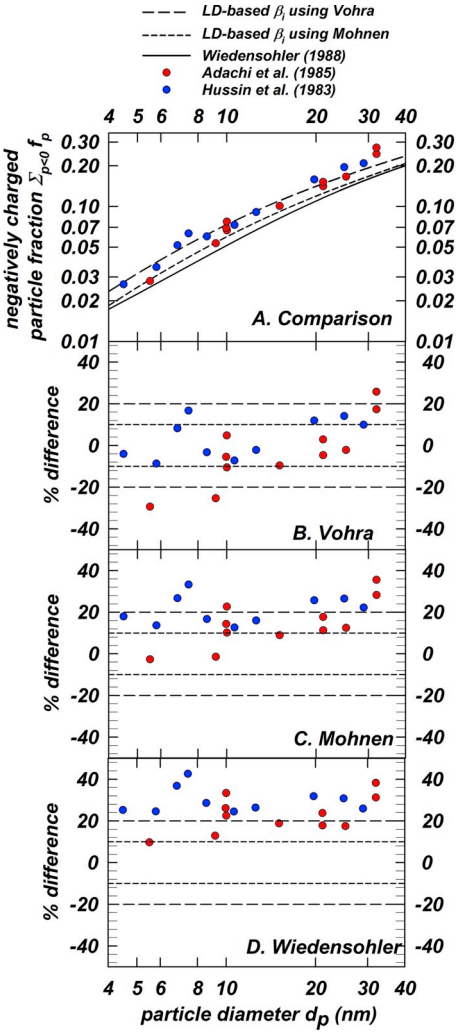

Fig. 11. A) Plot of the experimentally measured $\sum_{p=-\infty}^{p<0} f_p$ reported by Adachi et al. (1985), Kousaka et al. (1983) and Hussin et al. (1983) shown as data points of various colors and corresponding theoretical predictions (using eq. (7) & eq. (8) in eq. (10)) for two sets of ion properties (Mohnen and Vohra) shown as dashed black lines and Wiedensohler's regression (eq. (12)) as a solid black line. B) The % difference defined as $\left(1 - \frac{(\sum_{p=-\infty}^{p<0} f_p)_{eq.\ 7,eq.8,\ V}}{(\sum_{p=-\infty}^{p<0} f_p)_{exp}}\right)$ between predictions using Vohra's ion properties is plotted. C) The % difference defined as $\left(1 - \frac{(\sum_{p=-\infty}^{p<0} f_p)_{eq.\ 7,eq.8,\ M}}{(\sum_{p=-\infty}^{p<0} f_p)_{exp}}\right)$ between predictions using Mohnen's ion properties is plotted. D) The % difference defined as $\left(1 - \frac{(\sum_{p=-\infty}^{p<0} f_p)_{eq.\ 12}}{(\sum_{p=-\infty}^{p<0} f_p)_{exp}}\right)$ between Wiedensohler's regression is plotted. Reference lines are shown at ±10% and ±20%. The ion properties used in this plot are listed in Tables S5–A of the SI. (For interpretation of the references to color in this figure legend, the reader is referred to the Web version of this article.)

in panels 9-B (predictions using Vohra's ion properties) and 9-C (Mohnen's ion properties) of Fig. 9 with ±10% and ± 20% given for reference. Firstly, the data is seen to mostly fall within ±20%. The scatter in the % difference is symmetric about 0, indicating no apparent bias in the predictions. This establishes the accuracy but not precision of Langevin-based β_i models (eq. (7) and eq. (8)) for charging calculations. The scatter/lack of precision in the data is also partly due to experimental uncertainties, and the fact that the Langevin-based β_i models are able to capture the data accurately down to 4 nm indicates the utility of the model for sub-micron aerosol charging. Wiedensohler (1988) regression systematically underpredicts the experimental charged particle fractions up to 40%. The % difference is seen to increase for particle diameter $< 10\,nm$, especially. Wiedensohler's parameterization uses a fixed set of ion properties to calculate β_i and subsequently the charge fractions for $p = -2, -1, 0, 1, 2$. This parameterization neglects the possibility of charge levels beyond 3 for either polarity. At higher charge states, $|\Psi_E|$ could be as high as 60 for sub-20 nm particles. For such high values of $\Psi_E >> \frac{3}{2}$, Chahl and Gopalakrishnan (2019) showed that the limiting sphere approach (D'Yachkov et al., 2007) consistently underpredicts β_i for $Kn_D > 10$. Thus, based on this comparison we infer that for calculating charge distribution of sub-10 or sub-20 nm particles, the LD-based β_i (eqs. (7) and (8)) are more accurate than Wiedensohler's regression expression, especially if ion properties are measured simultaneously. Predicted and measured $\sum_{p>0}^{p=\infty} f_p$ shown in Fig. 10-A of Adachi et al. (1985) and Hussin et al. (1983)'s data again shows excellent agreement with most data points within ±10% (see Fig. 10-B and 10-C). Also shown in Fig. 10-A is the regression of eq. (12) that is nearly identical to the set of predictions using eq. (7) & Mohnen's ion properties. However, Fig. 11-A shows that $\sum_{p=-\infty}^{p<0} f_p$ experimental data are consistently higher than the predictions of eq. (12) (see Fig. 11-D). Fig. 11-B and 11-C show that LD-based β_i capture the data within ±20% nominally. This underprediction again confirms the systemic deficiencies of the limiting sphere approach at high Ψ_E. In unison, Figs. 9–11 show that bipolar charge distributions using eq. (7) and eq. (8) accurately reproduce Adachi et al. (1985)'s measurements (to within ±20% and that the corresponding predictions of Wiedensohler (1988) regression fall below the experiments for sub-40 nm particles.

Gopalakrishnan et al. (2015)'s charge distributions for 51.5 nm and 73.2 nm gold particles are presented in Table 2–A along with predictions for the same calculated using eq. (10) with β_i from eqs. (7) and (8), and with the ion properties listed in Tables S5–C. Comparison between measurements and predictions in ultrahigh purity (UHP) air reveals excellent agreement to within ±10% for both 51.5 nm and 73.2 nm particles. This shows that when ion properties are known accurately, LD-based models allow accurate and precise determination of charge fractions. The comparisons in carbon dioxide show higher % differences, especially for the ratios of $\frac{f_{p=+1}}{f_{p=+2}}, \frac{f_{p=-1}}{f_{p=+1}}, \frac{f_{p=-2}}{f_{p=+2}}$. We attribute this apparent anomaly to the fact that our bipolar charge distribution calculations assumed that positive and negative ions are only singly charged. Gopalakrishnan et al. (2015) state the possibility of the formation of doubly charged positive and negative ions by direct ionization of carbon dioxide due to higher electronegativity compared to nitrogen/oxygen. While we are not sure the precise reason for this high % difference in carbon dioxide, we also point out the $< \pm 5\%$ agreement of the neutral fraction of particles. Nevertheless, the LD-based β_i models (eq. (7) and eq. (8)) show excellent agreement with measurements in air, nitrogen, and argon. The disagreement in helium and carbon dioxide needs to be examined with attention to the nature of the ions formed in that gas as well

Table 2a
Table listing the experimentally measured charge distribution metrics reported by Gopalakrishnan et al. (2015) and corresponding theoretical predictions using the reported ion properties listed in Tables S5–C. The % difference between predictions and experiments for each quantity $(\cdot)$ is defined as $\left(1 - \frac{(\cdot)_{eq.\,7,eq.8}}{(\cdot)_{exp}}\right)$. Comparison is carried out for 51.5 nm and 73.2 nm gold particles in UHP Air and CO_2.

UHP Air	$d_p = 51.5\,nm$			$d_p = 73.2\,nm$		
	Measured	Predicted	% diff.	Measured	Predicted	% diff.
f_0	0.54	0.6030	− 12.63	0.48	0.5169	− 8.68
$\frac{f_{p=-1}}{f_{p=+1}}$	17.23	18.3827	− 6.68	7.64	8.5172	− 11.48
$\frac{f_{p=-2}}{f_{p=+1}}$	23.12	22.9647	0.68	9.87	10.4274	− 5.69
$\frac{f_{p=+2}}{f_{p=-1}}$	1.15	1.2255	− 6.78	1.24	1.2033	3.03
$\frac{f_{p=+1}}{f_{p=-2}}$	1.54	1.5309	0.36	1.60	1.4732	7.87
$\frac{f_{p=+2}}{f_{p=-2}}$						
CO_2	$d_p = 51.5\,nm$			$d_p = 73.2\,nm$		
	Measured	Predicted	% diff.	Measured	Predicted	% diff.
f_0	0.61	0.5943	3.12	0.48	0.5071	− 5.68
$\frac{f_{p=-1}}{f_{p=+1}}$	13.64	13.9536	− 2.28	6.46	6.7577	− 4.57
$\frac{f_{p=-2}}{f_{p=+1}}$	21.11	17.6573	16.36	9.10	8.3509	8.23
$\frac{f_{p=+2}}{f_{p=-1}}$	1.64	1.2358	24.48	2.19	1.2182	44.30
$\frac{f_{p=+1}}{f_{p=-2}}$	2.53	1.5638	38.29	2.19	1.5054	31.17
$\frac{f_{p=+2}}{f_{p=-2}}$						

as their mobilities taking into the polarization limit of ions near relatively large, polarizable gas molecules of carbon dioxide (compared to symmetric nitrogen/oxygen molecules).Table 2–B presents a comparison between the experimental data and the predictions of eq. (12). It is seen that Wiedensohler's model also explains the data well, in spite of the deficiencies noted previously. Limiting sphere approaches and LD-based approach yield similar values of β_i for $Kn_D < 10$ (charged particles that are greater than ~ 20 nm) is further vindicated by this agreement for ~50 nm and ~70 nm particles for which $Kn_D \tilde{} 0.5$ and $\Psi_E \tilde{} 2 - 4$. Fig. 12 presents $\Psi_E,\ Kn_D,\ \beta_i$ for the collisions between negatively charged 10, 50, 100 nm particles and N_2^+ ions in air (with conditions same as Fig. 8). Considering particle charge up to 5, it is seen that $[\Psi_E,\ Kn_D]$ varies up to ~[56, 2] for 10 nm particles, ~[11, 0.4] for 50 nm particles and ~[6, 0.2] for 100 nm particles. Fig. 12-C, D, E show that the LD-based (eq. (8)) and Fuchs-derived β_i (eq. (12)) differ very little from each other in these conditions. While Wiedensohler (1988), that uses collision kernel values derived from the limiting sphere approach (Hoppel & Frick, 1986), has been numerously used to calculate steady state bipolar charge distributions found in neutralizer/ambient ions, the presented set of LD-based β_i models (eqs. (7) and (8)) are applicable for wider range of charging conditions (plasma generated ions or charging at low or high pressures). Specifically, for sub-20 nm particles, the LD-based β_i (eqs. (7) and (8) in eq. (10)) are more accurate than Wiedensohler's expression (eq. (12)). Although Wiedensohler's regression was derived specifically for ions in air, it is erroneous usage in other gases should be avoided and the LD-based β_i may be used with appropriate ion properties.

The LD-based β_i model is based on the Langevin formulation to calculate particle-ion collision times and implicitly assumes that the ions are much heavier than the background gas molecules. Practically, this makes eq. (7) and eq. (8) applicable to describe the charging of ions heavier or at least of equal mass as the background gas molecules. The effect of dielectric constant of particle material, though expected to be small for dielectric constants >2.5 (Davison & Gentry, 1985), can be incorporated into the formulation of Ψ_I through eq. (2b). The presented approach by analyzing LD simulations is ideally suited for describing the bipolar charging of non-spherical particles as well. The effect of particle shape has been parameterized in prior studies (Gopalakrishnan et al., 2013a, 2013b, 2015) and will have to be experimentally validated in future studies. The presented β_i models (eq. (7) and eq. (8)) are valid for $0 < \Psi_E \leq 60$, $0 \leq \frac{\Psi_I}{\Psi_E} \leq 1$ and $Kn_D \leq 2000$. For most aerosol charging situations, $Kn_D \leq 20$ even for ~2 nm particles at atmospheric pressures. Thus, the presented models can be used to predict particle charging at low pressures as well. For a singly charged 2 nm particle at 300 K, $\Psi_E \tilde{} 56$. Thus, the presented model covers a broad range of particle charge and size as well as gas temperature and pressure. For ions formed in ambient condition by the ionization of molecules by low-energy radiation, electrical mobility is typically of the order of $10^{-4}\frac{m^2}{s.V}$ at atmospheric pressure and is thus well accommodated in the $Kn_D \leq 2000$ range examined in the model development. In summary, the presented LD-based β_i models (eq. (7) and eq. (8)) are shown to be accurate in qualitatively and quantitatively predicting unipolar and bipolar diffusion charging distributions.

4. Conclusions

From the described study aimed at developing and validating Langevin Dynamics (LD) based collision kernel β_i models for particle-ion diffusion charging in unipolar and bipolar ion environments, we derive the following conclusions:

1. We present a β_i accounting the particle-ion attractive Coulomb and image potential interactions that is accurate in describing the Langevin-inferred β_i from computations carried out following the approach of Chahl and Gopalakrishnan (2019). The developed model is valid for $0 < \Psi_E \leq 60,\ 0 \leq \frac{\Psi_I}{\Psi_E} \leq 1$ and $Kn_D \leq 2000$ that covers a broad range of aerosol diffusion charging conditions.
2. Eq. (7) and eq. (8) for β_i to describe particle-ion Coulomb and image potential interactions may be used to calculate unipolar (eq. (9)) and bipolar charge distributions (eq. (10)) accurately.
3. The LD-based β_i models are tested by comparing against experimentally measured charge distributions (both unipolar and bipolar). The comparisons with unipolar charging experiments establish the model's validity for in air, nitrogen and argon. Comparisons in helium are seen to be systematically lower than the experimental values, suggesting the need to probe unipolar charging further. Comparisons with bipolar charging experiments revealed that there is no apparent bias in the predictions and that with accurate determination of ion properties, LD-based β_i models yield excellent agreement with experimental data. The disagreement found in the case of bipolar charging in carbon dioxide needs to be further investigated, especially with respect to the possibility of multiply charged positive and negative ions involved in charging.
4. As part of this model validation, we chose to compare experimental results with current state-of-the-art Fuchs (1963) limiting sphere model for unipolar charging. It is seen that Fuchs' model and the LD-based model described here yield nearly identical predictions in the experimental conditions considered here for air, argon and nitrogen (Adachi et al., 1985, 1987). Further experiments at higher values of the $N_i\bar{t}$ parameter will be necessary to probe charging models at conditions of high potential energy (high Ψ_E) between the interacting particle and ion. The LD-based model and Fuchs model both underpredict charged particle fraction in helium, warranting further theoretical development for charging in helium.
5. Likewise, Wiedensohler (1988) regression was also compared against experimental data for bipolar charging (Adachi et al., 1985; Gopalakrishnan et al., 2015) along with the LD-based model. It is seen that usage of approximate ion properties and systemic issues in collision kernel prediction at high Ψ_E, lead to underprediction of the bipolar charged particle fraction and total fraction of negatively charged particles. Predictions by LD-based model and Wiedensohler's regression are accurate to predict bipolar charging in UHP air but not in carbon dioxide. Further work will be necessary to address this shortcoming of current charging models.
6. In summary, we have developed and validated a complete model for unipolar and bipolar diffusion charging of *spherical* aerosol particles in the *absence* of external fields. The model presented here may be used to investigate charging of particles (>2 nm) by

Table 2b
Table listing the experimentally measured charge distribution metrics reported by Gopalakrishnan et al. (2015) and corresponding theoretical predictions using the regression of Wiedensohler (1988). The % difference between predictions and experiments for each quantity $(\cdot)$ is defined as $\left(1-\frac{(\cdot)_{eq.\ 7,eq.8}}{(\cdot)_{exp}}\right)$. Comparison is carried out for 51.5 nm and 73.2 nm gold particles in UHP Air and CO_2.

UHP Air	$d_p = 51.5\ nm$			$d_p = 73.2\ nm$		
	Measured	Predicted	% diff.	Measured	Predicted	% diff.
f_0	0.54	0.5744	− 7.28	0.48	0.4932	− 3.70
$\frac{f_{p=-1}}{f_{p=+1}}$	17.23	18.1224	− 5.17	7.64	8.4564	− 10.68
$\frac{f_{p=-2}}{f_{p=+2}}$	23.12	23.7027	− 2.51	9.87	11.1295	− 12.81
$\frac{f_{p=+2}}{f_{p=-1}}$	1.15	1.291	− 12.48	1.24	1.2791	− 3.08
$\frac{f_{p=+1}}{f_{p=-2}}$	1.54	1.6885	− 9.89	1.60	1.6834	− 5.28
CO_2	$d_p = 51.5\ nm$			$d_p = 73.2\ nm$		
	Measured	Predicted	% diff.	Measured	Predicted	% diff.
f_0	0.61	0.5744	6.37	0.48	0.4932	− 2.77
$\frac{f_{p=-1}}{f_{p=+1}}$	13.64	18.1224	− 32.84	6.46	8.4564	− 30.85
$\frac{f_{p=-2}}{f_{p=+2}}$	21.11	23.7027	− 12.28	9.10	11.1295	− 22.31
$\frac{f_{p=+2}}{f_{p=-1}}$	1.64	1.2910	21.11	2.19	1.2791	41.51
$\frac{f_{p=+1}}{f_{p=-2}}$	2.53	1.6885	33.37	2.19	1.6834	23.03

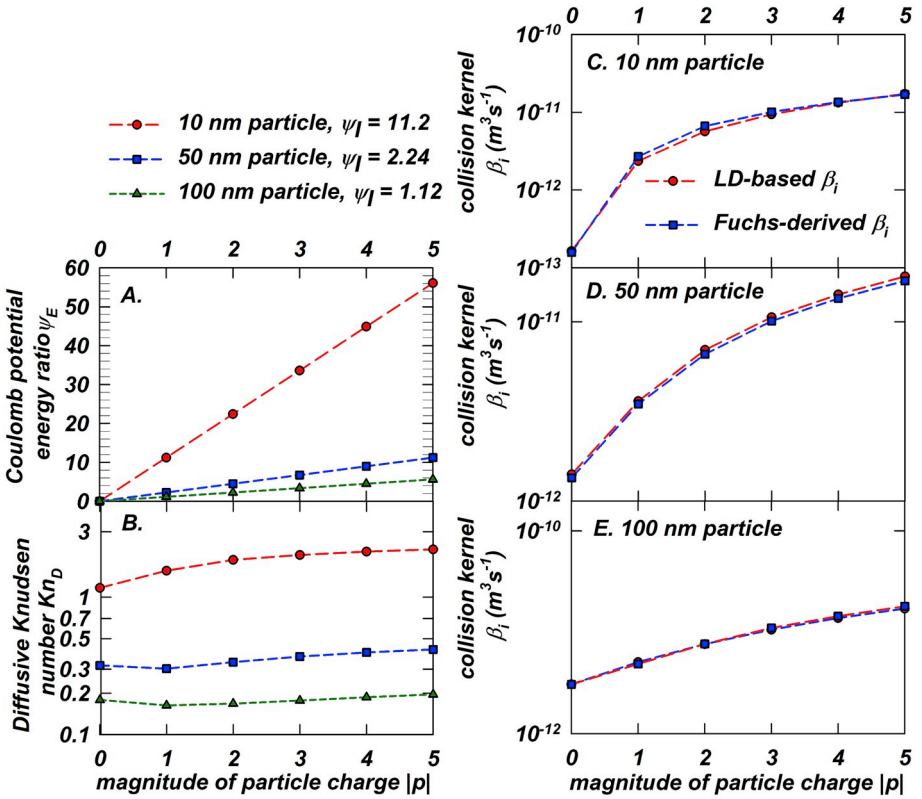

Fig. 12. Considering the collision between negatively charged 10, 50, 100 nm particles exposed to N_2^+ ions in N_2: A) Variation of the Coulomb potential energy ratio and B) the particle-ion diffusive Knudsen number as a function of the particle charge. Panels C, D, E show β_i predictions of LD model (eq. (8)) and Fuchs model (eq. (11)) for collisions between negatively charged particles carrying p units of charge and a positive ion.

molecular ions (that are of equal mass or heavier than the background gas, in gases other than helium and carbon dioxide) across a broad range of gas temperature and pressure, ion mass and mobility. The effect of particle shape, material, external electric fields and high ion concentrations (beyond the dilute limit) are also important and need to be examined in future modeling investigations.

Acknowledgements

We thank The University of Memphis High Performance Computing Cluster for providing computational resources to carry out this research. Funding for this work was provided by US National Science Foundation (NSF) PHY Grant Award Number 1903432 under the Directorate of Mathematical & Physical Sciences. We are indebted to our Editor Prof. Chris Hogan and one anonymous reviewer for guidance and comments in improving drafts of this manuscript during review.

Appendix A. Supplementary data

Supplementary data to this article can be found online at https://doi.org/10.1016/j.jaerosci.2019.105481.

References

Adachi, M., Kousaka, Y., & Okuyama, K. (1985). Unipolar and bipolar diffusion charging of ultrafine aerosol-particles. *Journal of Aerosol Science, 16*(2), 109–123.
Adachi, M., Okuyama, K., Kousaka, Y., Kozuru, H., & Pui, D. Y. H. (1987). Diffusion charging of ultrafine aerosol-particles by positive Helium, Argon, and Nitrogen-ions. *Journal of Applied Physics, 62*(7), 3050–3052. https://doi.org/10.1063/1.339368.
Adachi, M., Okuyama, K., Kousaka, Y., Kozuru, H., & Pui, D. Y. H. (1989). Bipolar diffusion charging of aerosol-particles under high particle ion concentration ratios. *Aerosol Science and Technology, 11*(2), 144–156. https://doi.org/10.1080/02786828908959307.
Allen, J. E. (1992). Probe theory - the orbital motion approach. [Article; proceedings paper]. *Physica Scripta, 45*(5), 497–503. https://doi.org/10.1088/0031-8949/45/5/013.
Biskos, G., Reavell, K., & Collings, N. (2005). Unipolar diffusion charging of aerosol particles in the transition regime. *Journal of Aerosol Science, 36*(2), 247–265. https://doi.org/10.1016/j.jaerosci.2004.09.002.
Boisdron, Y., & Brock, J. R. (1970). On the stochastic nature of the acquisition of electrical charge and radioactivity by aerosol particles, 1967 *Atmospheric Environment, 4*(1), 35–50. https://doi.org/10.1016/0004-6981(70)90052-1.
Bricard, J. (1962). La fixation des petits ions atmosphériques sur les aérosols ultra-fins. *Geofisica pura e applicata, 51*(1), 237–242. https://doi.org/10.1007/BF01992666.
Brock, J. R. (1970). Aerosol charging: The role of image force. *Journal of Applied Physics, 41*, 843–844.
Brock, J. R. (1970). Noncontinuum unipolar charging of aerosols: The role of external electric fields. *Journal of Applied Physics, 41*(5), 1940–1944. https://doi.org/10.1063/1.1659146.
Brock, J. R., & Wu, M.s. (1973). Field charging of aerosol particles. *Journal of Colloid and Interface Science, 45*(1), 106–114. https://doi.org/10.1016/0021-9797(73)90247-6.
Chahl, H. S., & Gopalakrishnan, R. (2019). High potential, near free molecular regime Coulombic collisions in aerosols and dusty plasmas. *Aerosol Science and Technology, 53*(8), 933–957. https://doi.org/10.1080/02786826.2019.1614522.
Chandrasekhar, S. (1943). Stochastic problems in physics and astronomy. *Reviews of Modern Physics, 15*, 1–89.
Chang, J. S., & Ono, S. (1987). Diffusion charging of nonspherical particles by bipolar ions under external magnetic fields. *Journal of Aerosol Science, 18*(6), 765–768. https://doi.org/10.1016/0021-8502(87)90117-0.
D'Yachkov, L. G., Khrapak, A. G., Khrapak, S. A., & Morfill, G. (2007). Model of grain charging in collisional plasmas accounting for collisionless layer. *Physics of Plasmas, 14*.
Davison, S. W., & Gentry, J. W. (1985). Differences in diffusion charging of dielectric and conducting ultrafine aerosols. *Aerosol Science and Technology, 4*(2), 157–163. https://doi.org/10.1080/02786828508959045.
Davison, S. W., Hwang, S. Y., Wang, J., & Gentry, J. W. (1985). Unipolar charging of ultrafine particles by diffusion of ions - theory and experiment. *Langmuir, 1*(1), 150–158. https://doi.org/10.1021/la00061a027.
Dawes, J. M., & Sceats, M. G. (1988). Biomolecular reactions on surfaces. Theory for arbitrary mean free path. *The Journal of Chemical Physics, 88*, 5489–5495.
Filippov, A. V. (1993). Charging of aerosol in the transition regime. *Journal of Aerosol Science, 24*(4), 423–436. https://doi.org/10.1016/0021-8502(93)90029-9.
Fjeld, R. A., Gauntt, R. O., & McFarland, A. R. (1981). Aerosol charging by bipolar ions of unequal current densities - experiments in low electric-fields. *Journal of Colloid and Interface Science, 83*(1), 82–89. https://doi.org/10.1016/0021-9797(81)90012-6.
Friedlander, S. K. (2000). *Smoke, dust, and haze: Fundamentals of aerosol dynamics, null*.
Fuchs, N. A. (1963). On the stationary charge distribution on aerosol particles in a bipolar ionic atmosphere. *Geofis. Pura Appl., 51*, 185–193.
Gatti, M., & Kortshagen, U. (2008). Analytical model of particle charging in plasmas over a wide range of collisionality. [Article]. *Physical Review E, 78*(4), 046402. https://doi.org/10.1103/PhysRevE.78.046402.
Gelbard, F., Tambour, Y., & Seinfeld, J. H. (1979). Sectional representations for simulating aerosol dynamics. *Journal of Colloid and Interface Science, 76*, 541–556.
Gopalakrishnan, R., & Hogan, C. J. (2011). Determination of the transition regime collision kernel from mean first passage times. *Aerosol Science and Technology, 45*, 1499–1509.
Gopalakrishnan, R., & Hogan, C. J. (2012). Coulomb-influenced collisions in aerosols and dusty plasmas. *Physical Review E, 85*, 026410.
Gopalakrishnan, R., McMurry, P. H., & Hogan, C. J. (2015). The bipolar diffusion charging of nanoparticles: A review and development of approaches for non-spherical particles. *Aerosol Science and Technology, 49*(12), 1181–1194. https://doi.org/10.1080/02786826.2015.1109053.
Gopalakrishnan, R., Meredith, M. J., Larriba-Andaluz, C., & Hogan, C. J. (2013). Brownian dynamics determination of the bipolar steady state charge distribution on spheres and non-spheres in the transition regime. *Journal of Aerosol Science, 63*, 126–145. https://doi.org/10.1016/j.jaerosci.2013.04.007.
Gopalakrishnan, R., Thajudeen, T., Ouyang, H., & Hogan, C. J., Jr. (2013). The unipolar diffusion charging of arbitrary shaped aerosol particles. *Journal of Aerosol Science, 64*(0), 60–80. https://doi.org/10.1016/j.jaerosci.2013.06.002.
Hagen, D. E., & Alofs, D. J. (1983). Linear inversion method to obtain aerosol size distributions from measurements with a differential mobility analyzer. *Aerosol Science and Technology, 2*(4), 465–475. https://doi.org/10.1080/02786828308958650, 10.1080/02786828308958650.
Hogan, C. J., Li, L., Chen, D. R., & Biswas, P. (2009). Estimating aerosol particle charging parameters using a Bayesian inversion technique. *Journal of Aerosol Science, 40*(4), 295–306. https://doi.org/10.1016/j.jaerosci.2008.11.008.
Hoppel, W. A., & Frick, G. M. (1986). Ion-aerosol attachment coefficients and the steady-state charge distribution on aerosols in a bipolar ion environment. *Aerosol Science and Technology, 5*(1), 1–21.

Hussin, A., Scheibel, H. G., Becker, K. H., & Porstendörfer, J. (1983). Bipolar diffusion charging of aerosol particles—I: Experimental results within the diameter range 4–30 nm. *Journal of Aerosol Science, 14*(5), 671–677.
Hwang, J., & Daily, J. W. (1992). A study of particle charging for electric field enhanced deposition. *Aerosol Science and Technology, 16*(2), 113–125. https://doi.org/10.1080/02786829208959542.
Hwang, S. Y., Gentry, J. W., & Davison, S. W. (1986). Unipolar charging of ultrafine aerosols. *Journal of Aerosol Science, 17*(2), 117–127. https://doi.org/10.1016/0021-8502(86)90059-5.
Jeong, J., & Choi, M. (2001). A sectional method for the analysis of growth of polydisperse non-spherical particles undergoing coagulation and coalescence. *Journal of Aerosol Science, 32*(5), 565–582. https://doi.org/10.1016/S0021-8502(00)00103-8.
Jackson, J. D. (1975). *Classical electrodynamics*. New York: John Wiley and Sons.
Kirsch, A. A., & Zagnit'Ko, A. V. (1981). Diffusion charging of submicrometer aerosol particles by unipolar ions. *Journal of Colloid and Interface Science, 80*(1), 111–117. https://doi.org/10.1016/0021-9797(81)90165-X.
Kirsch, A. A., & Zagnit'ko, A. V. (1990). Field charging of fine aerosol particles by unipolar Ions. *Aerosol Science and Technology, 12*(3), 465–470. https://doi.org/10.1080/02786829008959362.
Kousaka, Y., Adachi, M., Okuyama, K., Kitada, N., & Motouchi, T. (1983). Bipolar charging of ultrafine aerosol particles. *Aerosol Science and Technology, 2*(4), 421–427. https://doi.org/10.1080/02786828308958645.
Liu, B. Y. H., & Pui, D. Y. H. (1974). Equilibrium bipolar charge distribution of aerosols. *Journal of Colloid and Interface Science, 49*(2), 305–312. https://doi.org/10.1016/0021-9797(74)90366-X.
Liu, B. Y. H., & Pui, D. Y. H. (1977). On unipolar diffusion charging of aerosols in the continuum regime. *Journal of Colloid and Interface Science, 58*(1), 142–149. https://doi.org/10.1016/0021-9797(77)90377-0.
Liu, B. Y. H., Whitby, K. T., & Yu, H. H. S. (1967). Diffusion charging of aerosol particles at low pressures. *Journal of Applied Physics, 38*(4), 1592–1597. https://doi.org/10.1063/1.1709728.
Liu, B. Y. H., & Yeh, H. C. (1968). On the theory of charging of aerosol particles in an electric Field. *Journal of Applied Physics, 39*(3), 1396–1402. https://doi.org/10.1063/1.1656368.
Lopez-Yglesias, X., & Flagan, R. C. (2013). Ion-aerosol flux coefficients and the steady-state charge distribution of aerosols in a bipolar ion Environment. *Aerosol Science and Technology, 47*(6), 688–704. https://doi.org/10.1080/02786826.2013.783684.
Lushnikov, A. A., & Kulmala, M. (2004). Flux-matching theory of particle charging. *Physical Review E, 70*(4), 046413.
Maißer, A., Thomas, J. M., Larriba-Andaluz, C., He, S., & Hogan, C. J. (2015). The mass–mobility distributions of ions produced by a Po-210 source in air. *Journal of Aerosol Science, 90*, 36–50. https://doi.org/10.1016/j.jaerosci.2015.08.004.
Marlow, W. H. (1980). Derivation of aerosol collision rates for singular attractive contact potentials. *The Journal of Chemical Physics, 73*(12), 6284–6287. https://doi.org/10.1063/1.440126.
Marquard, A., Meyer, J., & Kasper, G. (2007). Unipolar field and diffusion charging in the transition regime - part II: Charging experiments. *Aerosol Science and Technology, 41*(6), 611–623. https://doi.org/10.1080/02786820701272061.
McMurry, P. H. (2000). A review of atmospheric aerosol measurements. *Atmospheric Environment, 34*(12–14), 1959–1999.
Mohnen, V. A. (1974). Formation, nature, and mobility of ions of atmospheric importance. In H. Dolezalek, & R. Reiter (Eds.), *Electrical processes in atmospheres - proceedings of the fifth international conference on atmospheric electricity held at Garmisch-Partenkirchen (Germany), 2–7 September 1974*. Steinkopff-Verlag Heidelberg.
Mott-Smith, H. M., & Langmuir, I. (1926). The theory of collectors in gaseous discharges. *Physical Review, 28*(4), 727–763.
O'Hara, D. B., Clements, J. S., Finney, W. C., & Davis, R. H. (1989). Aerosol particle charging by free electrons. *Journal of Aerosol Science, 20*(3), 313–330. https://doi.org/10.1016/0021-8502(89)90007-4.
Oh, H., Park, H., & Kim, S. (2004). Effects of particle shape on the unipolar diffusion charging of nonspherical particles. *Aerosol Science and Technology, 38*(11), 1045–1053. https://doi.org/10.1080/027868290883324, 10.1080/027868290883324.
Ouyang, H., Gopalakrishnan, R., & Hogan, C. J., Jr. (2012). Nanoparticle collisions in the gas phase in the presence of singular contact potentials. *The Journal of Chemical Physics, 137*(6), 064316. https://doi.org/10.1063/1.4742064.
Porstendorfer, J., Hussin, A., Scheibel, H. G., & Becker, K. H. (1984). Bipolar diffusion charging of aerosol-particles .2. Influence of the concentration ratio of positive and negative-ions on the charge distribtuion. [Article]. *Journal of Aerosol Science, 15*(1), 47–&. https://doi.org/10.1016/0021-8502(84)90055-7.
Porstendörfer, J., Hussin, A., Scheibel, H. G., & Becker, K. H. (1984). Bipolar diffusion charging of aerosol particles—II. Influence of the concentration ratio of positive and negative ions on the charge distribution. *Journal of Aerosol Science, 15*(1), 47–56. https://doi.org/10.1016/0021-8502(84)90055-7.
Pui, D. Y. H., Fruin, S., & McMurry, P. H. (1988). Unipolar diffusion charging of ultrafine aerosols. *Aerosol Science and Technology, 8*(2), 173–187. https://doi.org/10.1080/02786828808959180.
Reischl, G. P., Mäkelä, J. M., Karch, R., & Necid, J. (1996). Bipolar charging of ultrafine particles in the size range below 10 nm. *Journal of Aerosol Science, 27*(6), 931–949. https://doi.org/10.1016/0021-8502(96)00026-2.
Reischl, G. P., Scheibel, H. G., & Porstendörfer, J. (1983). The bipolar charging of aerosols: Experimental results in the size range below 20-nm particle diameter. *Journal of Colloid and Interface Science, 91*(1), 272–275. https://doi.org/10.1016/0021-9797(83)90332-6.
Rogak, S. N., & Flagan, R. C. (1992). Bipolar diffusion charging of spheres and agglomerate aerosol particles. *Journal of Aerosol Science, 23*(7), 693–710. https://doi.org/10.1016/0021-8502(92)90037-V.
Romay, F. J., & Pui, D. Y. H. (1992). Free-electron charging of ultrafine aerosol-particles. *Journal of Aerosol Science, 23*(7), 679–692. https://doi.org/10.1016/0021-8502(92)90036-U.
Romay, F. J., Pui, D. Y. H., & Adachi, M. (1991). Unipolar diffusion charging of aerosol-particles at low-pressure. *Aerosol Science and Technology, 15*(1), 60–68. https://doi.org/10.1080/02786829108959513.
Sceats, M. G. (1986). Brownian coagulation in a field of force. *The Journal of Chemical Physics, 84*, 5206–5208.
Sharma, G., Wang, Y., Chakrabarty, R., & Biswas, P. (2019). Modeling simultaneous coagulation and charging of nanoparticles at high temperatures using the method of moments. *Journal of Aerosol Science, 132*, 70–82. https://doi.org/10.1016/j.jaerosci.2019.03.011.
Stober, J., Schleicher, B., & Burtscher, H. (1991). Bipolar diffusion charging of particles in noble gases. *Aerosol Science and Technology, 14*(1), 66–73. https://doi.org/10.1080/02786829108959471, 10.1080/02786829108959471.
Thajudeen, T., Gopalakrishnan, R., & Hogan, C. J. (2012). The collision rate of non-spherical particles and aggregates for all diffusive knudsen numbers. *Aerosol Science and Technology, 46*(11).
Unger, L., Boulaud, D., & Borra, J. P. (2004). Unipolar field charging of particles by electrical discharge: Effect of particle shape. *Journal of Aerosol Science, 35*(8), 965–979. https://doi.org/10.1016/j.jaerosci.2004.01.006.
Vaulina, O. S., Repin, A. Y., & Petrov, O. F. (2006). Empirical approximation for the ion current to the surface of a dust grain in a weakly ionized gas-discharge plasma. *Plasma Physics Reports, 32*(6), 485–488. https://doi.org/10.1134/S1063780X06060055.
Vincenti, W. G., & Kruger, C. H. (1975). *Introduction to physical gas dynamics*. Huntington, NY: Krieger.
Vohra, K. G., Subbaramu, M. C., & Vaseduvam, K. N. (1969). *Nucleation of water cluster ions*. Bombay: Bhabha Atomic Research Center.
Wiedensohler, A. (1988). An approximation of the bipolar charge-distribution for particles in the sub-micron size range. *Journal of Aerosol Science, 19*(3), 387–389.
Wiedensohler, A., & Fissan, H. J. (1988). Aerosol charging in high-purity gases. *Journal of Aerosol Science, 19*(7), 867–870. https://doi.org/10.1016/0021-8502(88)90054-7.
Wiedensohler, A., Lutkemeier, E., Feldpausch, M., & Helsper, C. (1986). Investigation of the bipolar charge-distribution at various gas conditions. [Article]. *Journal of Aerosol Science, 17*(3), 413–416. https://doi.org/10.1016/0021-8502(86)90118-7.

Wu, J. J., & Flagan, R. C. (1988). A discrete-sectional solution to the aerosol dynamic equation. *Journal of Colloid and Interface Science, 123*(2), 339–352.
Ziemann, P. J., Kittelson, D. B., & McMurry, P. H. (1996). Effects of particle shape and chemical composition on the electron impact charging properties of submicron inorganic particles. *Journal of Aerosol Science, 27*(4), 587–606. https://doi.org/10.1016/0021-8502(96)00010-9.
Ziemann, P. J., Liu, P., Kittelson, D. B., & McMurry, P. H. (1995). Electron impact charging properties of size-selected, submicrometer organic particles. *The Journal of Physical Chemistry, 99*(14), 5126–5138. https://doi.org/10.1021/j100014a037.